Spin-polarized Oxygen Evolution Reaction under Magnetic Field

Xiao Ren[1,2], Tianze Wu[1,2,3], Yuanmiao Sun[2], Yan Li[1], Guoyu Xian[1], Xianhu Liu[4], Chengmin Shen[1], Jose Gracia[5], Hong-Jun Gao[1], Haitao Yang[1]*, Zhichuan J. Xu[2,3,6]*

[1] Beijing National Laboratory for Condensed Matter Physics and Institute of Physics, Chinese Academy of Science, P.O.Box 603, Beijing, 100190, China;

[2] School of Material Science and Engineering, Nanyang Technological University, 50 Nanyang Avenue, Singapore 639798, Singapore;

[3] Solar Fuels Laboratory, Nanyang Technological University, 50 Nanyang Avenue, Singapore 639798, Singapore;

[4] Key Laboratory of Advanced Material Processing & Mold (Zhengzhou University), Ministry of Education, Zhengzhou 450002, China;

[5] MagnetoCat SL, General Polavieja 9 3I, 03012 Alicante, Spain;

[6] Energy Research Institute @ Nanyang Technological University, 50 Nanyang Avenue, Singapore 639798, Singapore.

E-mails: xuzc@ntu.edu.sg; htyang@iphy.ac.cn

18

Abstract

The oxygen evolution reaction (OER) is the bottleneck that limits the energy efficiency of water-splitting. The process involves four electrons' transfer and the generation of triplet state O_2 from singulet state species (OH$^-$ or H_2O). Recently, explicit spin selection was described as a possible way to promote OER in alkaline conditions, but the specific spin-polarized kinetics remains unclear. Here, we report that by using ferromagnetic ordered catalysts as the spin polarizer for spin selection under a constant magnetic field, the OER can be enhanced. However, it does not applicable to non-ferromagnetic catalysts. We found that the spin polarization occurs at the first electron transfer step in OER, where coherent spin exchange happens between the ferromagnetic catalyst and the adsorbed oxygen species with fast kinetics, under the principle of spin angular momentum conservation. In the next three electron transfer steps, as the adsorbed O species adopt fixed spin direction, the OER electrons need to follow the Hund rule and Pauling exclusion principle, thus to carry out spin polarization spontaneously and finally lead to the generation of triplet state O_2. Here, we showcase spin-polarized kinetics of oxygen evolution reaction, which gives references in the understanding and design of spin-dependent catalysts.

35

Introduction

The sluggish kinetics of oxygen evolution reaction (OER) is a major cause for the low efficiency in techniques such as solar water splitting,[1] rechargeable metal-air batteries,[2] regenerative fuel cells,[3] and water electrolysis.[4, 5] Exploring better catalysts for OER has become increasingly attractive in recent years. Non-precious 3d-transition metal oxides (TMOs), such as Fe-, Co-, and Ni-based oxides, are promising cost-effective catalysts.[6, 7] Their catalytical activities are tunable as the diversity in oxides families affords numerous freedoms to tailor their physicochemical properties. Sabatier's principle, which qualitatively describes that the optimized catalytic activity when adsorbed species bind to the catalytic surface neither too strongly nor too weakly, led to the fundamental understanding of OER mechanisms and guided the subsequent design of highly active catalysts.[8, 9] This principle was further supported by the findings that the OER activities of transition metal oxides correlate strongly with the e_g occupancy, which is related to the binding strength between the metal and the oxygen species.[10-12] Some exceptions have been found not well fitted with the e_g theory, which is partially resulted by the diverse and complicated magnetism in TMOs family.[13-16] Besides, the produced O_2 is in triplet ground state, where the frontier π^* orbitals are occupied by two electrons with parallel alignment. In contrast, the ground spin state of reactant OH^-/H_2O is singlet with all paired electrons.[17, 18] The singlet states of the oxygen molecule were reported at an energy level of at least ~ 1 eV higher than its triplet state.[18, 19] Thus, the magnetism of TMOs, related to the spin polarization, should be influential on the kinetics of OER.[20, 21] It is reasonable to consider that the active sites with suitable thermodynamic paths for OER should allow a way to facilitate the spin alignment in the product. As suggested by recent theoretical studies by J. Gracia,[22-24] the spin-polarized electrons in catalysts promote the generation of parallel spin aligned oxygen by quantum spin-exchange interactions (QSEI), which further promote the OER kinetics. Therefore, facilitating the spin polarization should be an effective strategy for improving OER efficiency. Ron Naaman and co-works reported that the application of the chiral-induced spin selectivity effect to product the polarized electron. This spin polarization transferred is the origin of a more efficient oxidation process in which oxygen is formed in its triplet ground state.[25-27] It has been pointed out by J. Gracia et al. that theoretically photosystem II can act as

65   a spin-controlling gate to govern the charge and spin transport during the OER process,[28] which

66   offers a favoured thermodynamic path for O_2 evolution. Besides the extrinsic spin polarizer, the

67   ordered magnetic moment structure in ferromagnetic materials can create intrinsic spin filtering

68   for highly spin-polarized electrons. The spin filtering effect originates from the exchange

69   splitting of the energy levels in the conduction band of a magnetic insulator.[29] Most recently,

70   José Ramón Galán-Mascarós et al. reported an external magnetic field, applied by a permanent

71   magnet, enhances the OER activity of magnetic oxides in alkaline.[30] It opens a new strategy to

72   manipulate the spin polarization in magnetic oxide catalysts for promoting the OER and

73   encourages more detailed studies to understand how the magnetic field induced spin

74   polarization affects the OER process.

75   In this work, we report an investigation on the key kinetics change on the ferromagnetic

76    $CoFe_2O_4$ catalyst under the magnetic field. The ferromagnetic $CoFe_2O_4$ catalyst works as a spin

77   polarizer under the magnetic field. We have found that the spin-polarized kinetics of OER starts

78   at the first electron transfer step, where ferromagnetic exchange happens between the

79   ferromagnetic catalysts and the adsorbed oxygen species (reactants) under the principle of spin

80   angular momentum conservation. Without the magnetic field, the Tafel slope of $CoFe_2O_4$ is

81   identical and equal to circa 120 mV/decade, which indicates the first electron transfer step is

82   rate-determining step (RDS) and no electron transfer occurring before the RDS. Under the

83   magnetic field, the Tafel slope decreases to circa 90 mV/decade, indicating the number of

84   electron transfer is ~0.5 and a mixed RDS involving the first electron transfer step and second

85   steps. Such a phenomenon cannot be observed in the catalysts without ferromagnetic orderings

86   under the same condition. The results indicate that the key step of spin-polarized OER is the

87   first electron transfer step in OER, where the spin-polarized process via exchange hopping can

88   be facilitated under the magnetic field. As a consequence, the first electron transfer is no longer

89   the RDS. After a facilitated spin-polarized ferromagnetic exchange of electrons, the adsorbed

90   O species will overall settle on the fixed spin direction. Due to the Hund Rule and Pauli

91   Exclusion Principle, the follow-up electrons' transfer needs to carry out spin polarization

92   spontaneously and finally lead to the generation of triplet state oxygen. Overall, we showcase

93 the key kinetics information in OER under a magnetic field, which influences the micro- and

94 macroscopic spin-polarization and spin-transport. This finding will be helpful for further

95 development of magnetic-field assisted OER-enhancing strategy and related catalysts.

96

97

98 **Results and discussion**

99 **Magnetic and electrochemical characterizations**

100 We begin with the discussion of the magnetic properties of the employed catalysts, $CoFe_2O_4$,

101 Co_3O_4, and IrO_2. The study will determine the suitable magnetic field and weather a global

102 aligned magnetic moment can be achieved. The study of magnetic property reveals the optimal

103 strength of the applied magnetic field for the alignment of the magnetic moment in

104 ferromagnetic $CoFe_2O_4$. The $CoFe_2O_4$ and Co_3O_4 were prepared by a modified solid-state

105 chemistry method as previously reported.[11] X-ray powder diffraction characterization was

106 performed to confirm their crystal structures. The diffraction patterns match well with the

107 standard patterns without impurity peak found (Supplementary Figure 1 and Supplementary

108 Table 1).   As depicted in Figure 1a, $CoFe_2O_4$ gives a hysteresis loop in an enlarged manner,

109 indicating a room-temperature ferromagnetic behavior with a saturation magnetization (Ms) of

110 44 emu·g^{-1}. The Co_3O_4 and IrO_2 samples with tiny susceptibility (χ) of 3.07×10^{-5} and 0.51×10^{-6},

111 respectively, at 300 K show antiferromagnetic or paramagnetic behaviors, respectively. The

112 detailed magnetic data are summarized in Supplementary Table 1. The cyclic voltammetry (CV)

113 of those catalysts were then measured with and without a constant magnetic field of 10000 Oe

114 under alkaline condition (see Methods for details). As shown in Figure 1b, c, and d, the OER

115 performance of the ferromagnetic $CoFe_2O_4$ is promoted obviously under the magnetic field

116 while the changes in non-ferromagnetic catalysts Co_3O_4 and IrO_2 are negligible. When a strong

117 enough magnetic field (higher than the coercivity) is applied to a ferromagnetic material, the

118 magnetic moment will (macroscopically) align along with the direction of the external magnetic

119 field. The ferromagnetic (long-) ordered material as spin polarizer is an extended selective spin-

120 filter for electron transfer during catalysis. The generation process of polarized electrons has

121 been illustrated in Figure 1e.

122 It should be noticed that the use of magnetic fields in water electrolysis has been studied in the

123 past,[31-36] in which the mass transport in the electrochemical process was found to be affected

124 by the Lorentzian movement, i.e. the diffusion of regents and the release of the generated gas

125 bubbles are promoted. However, in this study, some evidence has excluded such effect from

126 mass transport as a main contributor to OER enhancement under the magnetic field. First, the

127 improvement was not observed on non-ferromagnetic catalysts Co_3O_4 and IrO_2 with the effect

128 of Lorentzian movement on mass transport. Second, we also tested the OER performance of

129 $Co(acac)_2$ and $Fe(acac)_3$ with and without a constant magnetic field (as shown in Supplementary

130 Figure 2). Nearly no difference can be observed. It also should be noted that OH^- and H_3O^+ in

131 aqueous solution do not move physically, but by sequential proton transfer, known as Grotthuss

132 mechanisms (Supplementary Figure 3). That means the influence of Lorentz force on the

133 physical movement of ions OH^- or H_3O^+ is negligible[37]. Thus, the effect from the mass transport

134 under the external magnetic field should have little contribution to the observed OER

135 enhancement of the ferromagnetic $CoFe_2O_4$. Besides, the electrical resistance of magnetic

136 materials can be affected by the magnetization, which is through the scattering of electrons on

137 the magnetic lattice of the crystal.[38-40] However, the difference in the conductivity at room

138 temperature under 10000 Oe is about 3% for insulator $CoFe_2O_4$ with 3.86×10^{-5} S/m,[40-42] which

139 does not cause a significant difference in the electrode's conductivity. This is because acetylene

140 black carbon (AB) with 500 S/m as a conductive mediator is mixed with those oxide catalysts

141 for their application as the electrode,[43] which dominants the electron conduction.
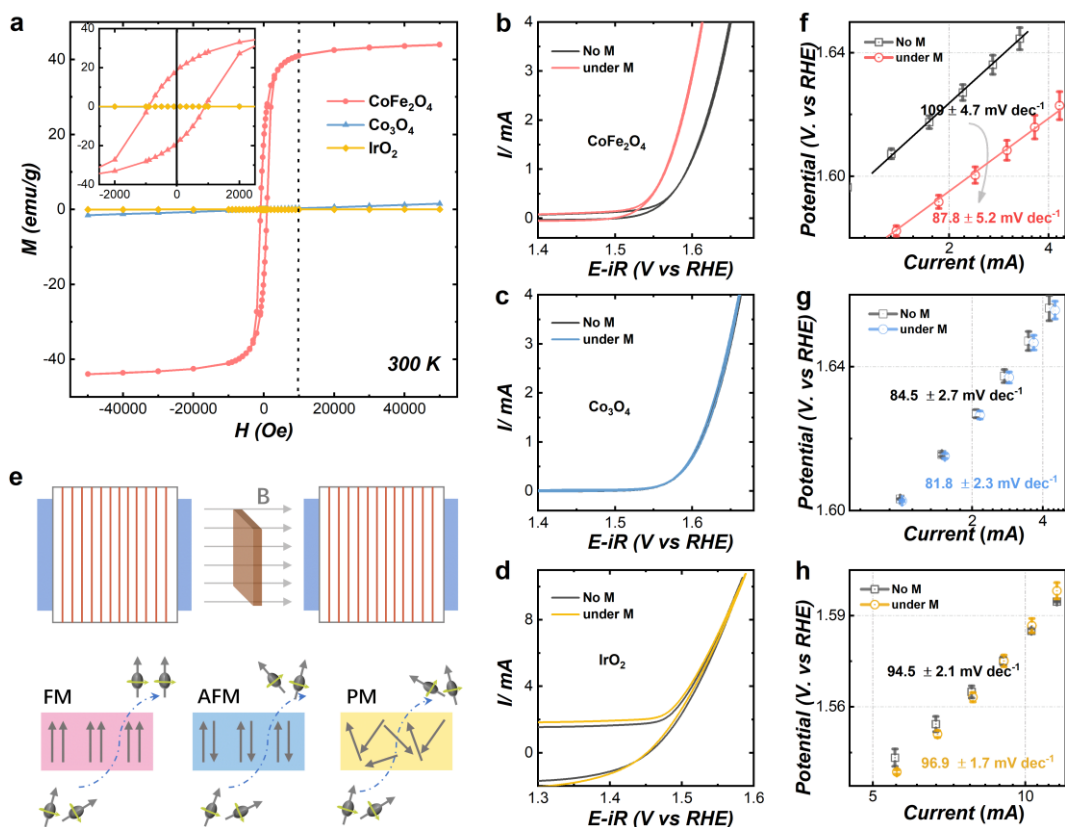
Figure 1 | Spin polarization promotes OER. (**a**) Magnetic hysteresis loops of $CoFe_2O_4$, Co_3O_4, and IrO_2 powders at room temperature (300 K) and the magnified graph inset in the top left of this panel. (Here, IrO_2 powder is a commercial catalyst (bulk, Premetek). Cyclic voltammetry (CV) of $CoFe_2O_4$ (**b**), Co_3O_4 (**c**), and IrO_2 (**d**) catalysts at a scan rate of 10 mV/s in O_2-saturated 1 M KOH with and without a constant magnetic field (10000 Oe). (**e**) The schematic of the generation of the polarized electron under a constant magnetic field. The Tafel plots of $CoFe_2O_4$, (**f**) Co_3O_4 (**g**), and IrO_2 (**h**) catalysts with and without a constant magnetic field (10000 Oe). The error bar represents three independent tests.

No surface restructuration in OER

It is generally recognized that some Co-based perovskites and spinels undergo operando surface reconstruction to form active Co (oxy) hydroxides in alkaline conditions to promote OER.[44-46] In our case, there are no changes in OER performance of $CoFe_2O_4$ during CA tests in 1 M KOH for 1 h shown in Supplementary Figure 4, indicating $CoFe_2O_4$ is stable without noticed surface reconstruction during the OER process. The high-resolution transmission electron microscope

158 (HRTEM) was further used to rule out the possible interference from surface reconstruction of

159 catalysts during the OER. It has been found that the spinel crystal structure of $CoFe_2O_4$

160 remained after the electrochemical treatment (Supplementary Figure 5), which is consistent

161 with what has been reported previously.[47] The aberration-corrected STEM provides direct

162 atomic imaging and confirms that the well-crystalline feature reserved from the surface to bulk

163 (Figure 2a, b). The HADDF line profile shows the same bond length of Co-O in bulk and

164 surface, which verifies no surface reconstruction (Figure 2c). Raman technique was then

165 performed to study the inhomogeneity evolution in the near-surface region. The Raman spectra

166 of cubic structures (Fd-3m) $CoFe_2O_4$ before and after OER are presented in Figure 2d. In the

167 top curve, peak maxima at 603 and 666 cm^{-1} are due to A_{1g} symmetry involving symmetric

168 stretching of oxygen atom with respect to the metal ions in tetrahedral sites. The other low-

169 frequency phonon modes are due to metal ions involved in octahedral sites, i.e., E_g and T_{1g}. The

170 assignment of these phonon modes was carried out in accordance with the literature.[48] After

171 electrochemical treatment (bottom curve), no changes in the vibrational modes were observed,

172 which proves once again that there is no surface reconstruction in OER. X-ray photoelectron

173 spectroscopy (XPS) was also performed to study the surface chemical states of $CoFe_2O_4$ before

174 and after the OER. As shown in Supplementary Figure 6, the XPS survey spectra confirm the

175 coexistence of Co, Fe, and O in the samples. Figure 2e shows the 2p orbital of Fe, Co, and 1s

176 orbital of O. The XPS of Fe 2p core level presents two pairs of peaks: Fe^{3+} $2p_{3/2}$ at about 710.7

177 eV and 713.2 eV; Fe^{3+} $2p_{1/2}$ at about 724.1 eV and 726.2 eV. The doublets in samples can be

178 ascribed to Fe^{3+} in octahedral sites and Fe^{3+} in tetrahedral sites, respectively. The two peaks of

179 Co 2p with the binding energy of 780.1 and 782.0eV are ascribed to Co^{2+} ions in octahedral

180 sites and Co^{2+} ions in tetrahedral sites. The main peaks of O 1s at 529.6 eV are recognized as

181 oxygen ions, which are all associated with a "-2" formal charge.[49] Compared to the spectra

182 before and after the OER, these peaks remain unchanged in location, indicating no surface

183 reconstruction.

184
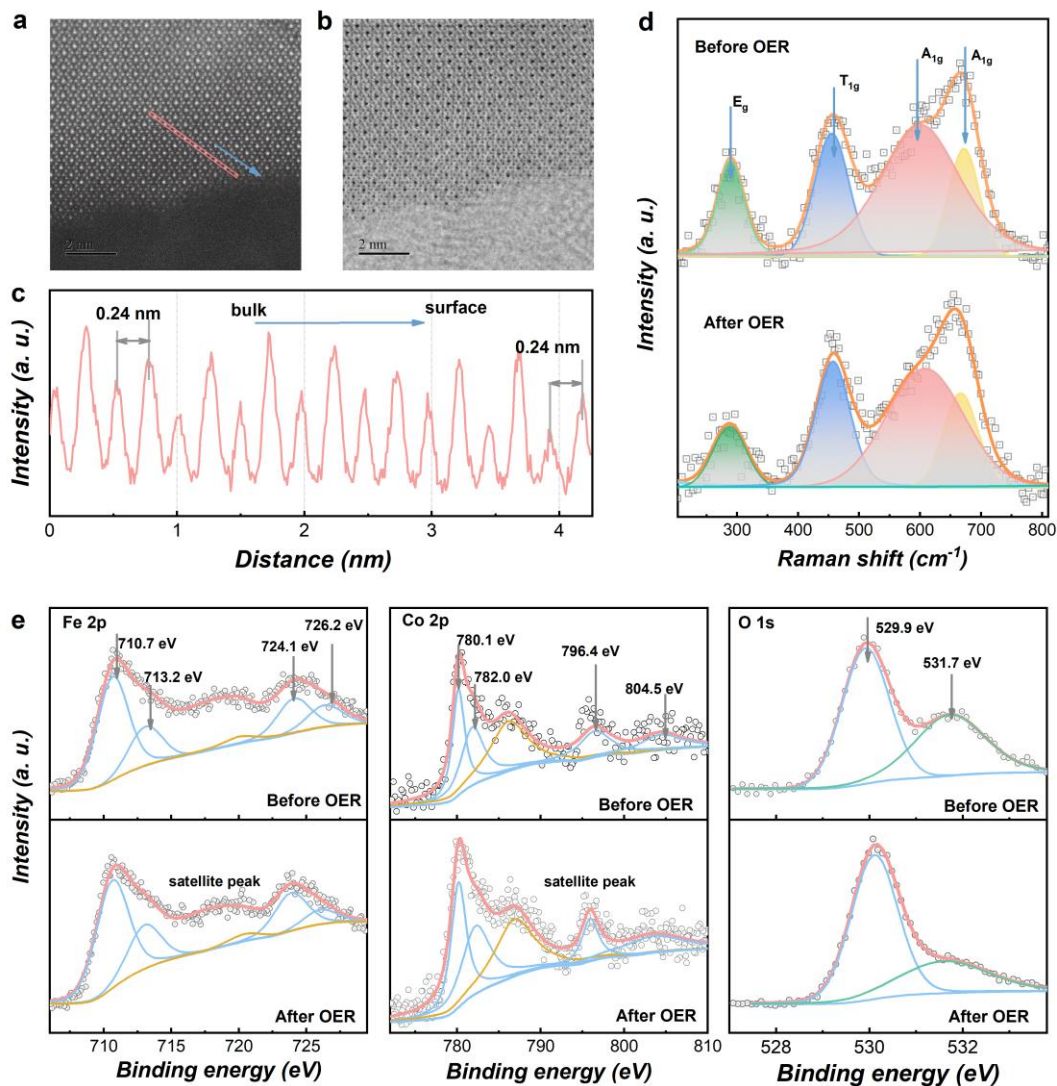
Figure 2 | No surface restructuration on CoFe$_2$O$_4$. HADDF (**a**) and ABF (**b**) images of CoFe$_2$O$_4$ after OER. The line profiles of HADDF (**c**) acquired at the pink line rectangular zone. (**d**) Raman spectra of CoFe$_2$O$_4$ before and after OER. (**e**)The Fe 2p, Co 2p and O 1s XPS spectra results of CoFe$_2$O$_4$ before and after OER.

Spin-polarized Kinetics of OER

Oxygen evolution reaction is authenticated a four-step reaction with each step accompanied by an electron transfer as shown in the top of Figure 4a. The Tafel plots are widely regarded as a generalized kinetics theory for electron transfer reactions. The Tafel equation presents the relationship between the Tafel slope and the exchange current density:

$$\eta = -\frac{2.303\,RT}{\alpha F} * log\,i_0 + \frac{2.303\,RT}{(\alpha + n)F} * log\,i$$

where the Tafel slope equals to $2.303RT/[(\alpha+n)F]$ (i_0 is the exchange current density, R is the universal gas constant, T is the absolute temperature, F is the Faraday constant, n is the number of electrons transferred before RDS, and α is the charge transfer coefficient and usually assumed to be 0.5).[50, 51] Ideally, the Tafel slope tells the information of reaction kinetics. For example, the Tafel slope is 120 mV·dec^{-1}, which indicates the first electron transfer step is the RDS because there is no electron transfer before the RDS. If the second step is the RDS, the Tafel slope will decrease to 40 mV·dec^{-1} with an electron transfer number of 1. The change of the Tafel slope is often reputed as an indication of the change of reaction mechanism. As shown in Figure 1f, the Tafel slope of $CoFe_2O_4$ is about 109 ± 4.7 mV·dec^{-1} and that indicates the first electron transfer from the adsorbed OH$^-$ is the RDS without the magnetic field. But, after applying a constant magnetic field, the Tafel slope decreases to circa 87.8 ± 5.2 mV·dec^{-1}, indicating the number of electron transfer is about 0.5 and a mixed RDS involving the first electron transfer step and second steps. Furthermore, we have carried out OER measurements of $CoFe_2O_4$, Co_3O_4, and IrO_2 under different temperatures as shown in Figure 3a. We first noted that the OER performance of catalysts is getting better as the reaction temperature increases. This is probably because that the rate constant of the reaction will increase as the reaction temperature increases, which can promote this reaction based on the transition state theory[52]. More importantly, the OER performance of the ferromagnetic $CoFe_2O_4$ is promoted under the magnetic field at various temperature. However, the positive influence of the magnetic field on the OER performance of $CoFe_2O_4$ is decreased as the reaction temperature increases. The corresponding Tafel slopes are shown in Figure 3b. At room temperature, the Tafel slope of $CoFe_2O_4$ is about 106 mV·dec^{-1} without the magnetic field. After applying a constant field, the Tafel slope decreases to circa 82.8 mV·dec^{-1}. As the temperature increases, the positive influence of the magnetic field became not that remarkable. This is because the arrangement of magnetic moments of catalyst will be thermally disturbed. The ferromagnetic ordering in the catalyst gets disturbed and thus a certain degree of demagnetization at high temperature occurs, which lead to the decreased influence of the magnetic field on OER. We also note that the Tafel

10

slope of $CoFe_2O_4$ have a slight favorable change as temperature increases, which maybe because   the interaction between two M-O unites mechanism occurs at high temperature.[53, 54] Thus, the key step in spin-polarized OER is the first electron transfer step in FM $CoFe_2O_4$, where the adsorbed OH^- is difficult to deprotonate and transfer the electron. However, the change of Tafel slopes was not observed in the non-ferromagnetic catalysts under the same condition.
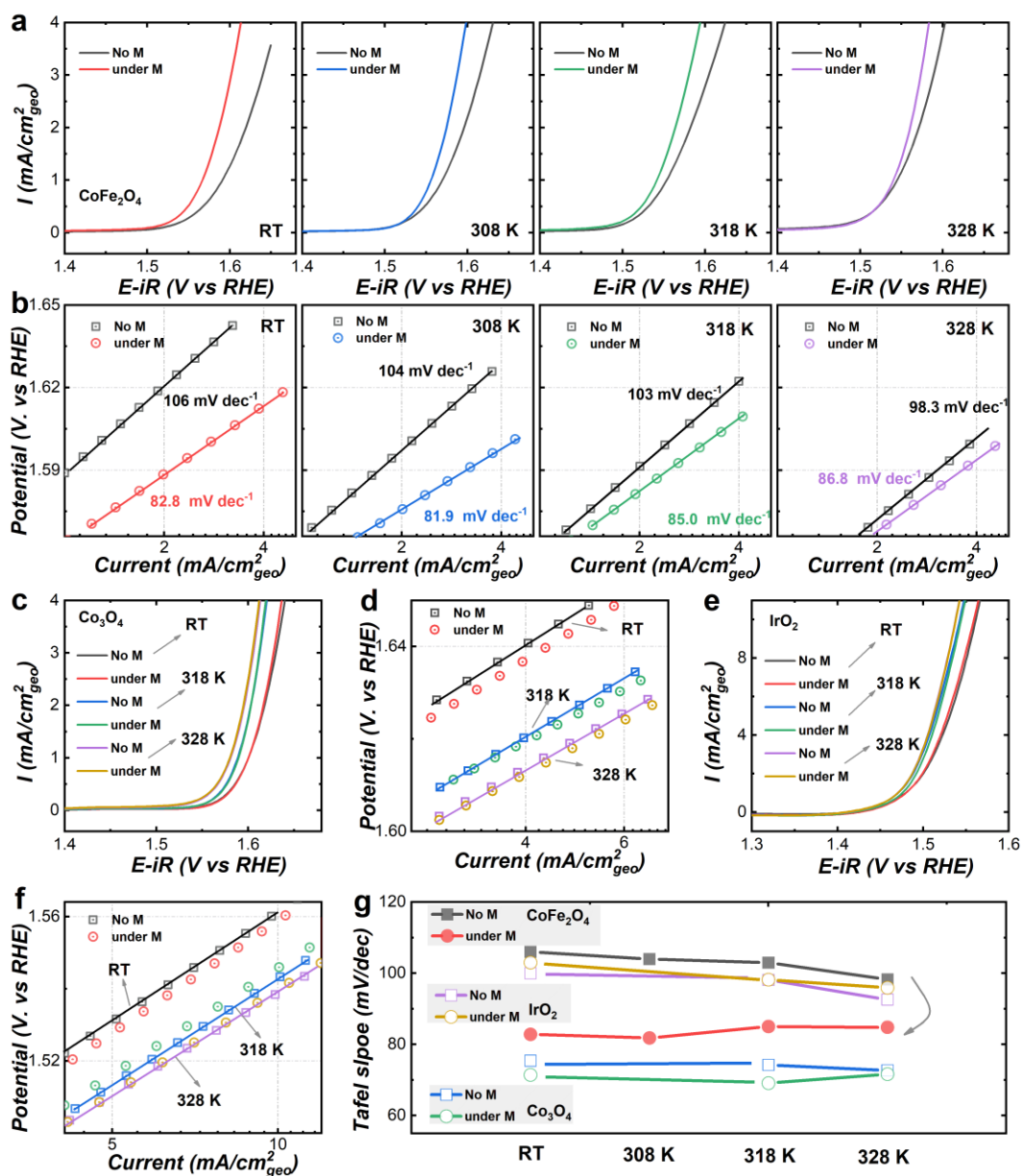
Figure 3 | OER under the different temperature. (**a**) LSV curves of $CoFe_2O_4$ at a scan rate of 10 mV/s in O_2-saturated 1 M KOH with and without a constant magnetic field (10000 Oe)

233 under the different temperatures (room temperature (RT): ~303 K, 308 K, 318K and 328 K).

234 The corresponding Tafel plots are shown in (**b**). (**c**) LSV curves of Co_3O_4 with and without a

235 constant magnetic field (10000 Oe) under the different temperatures (room temperature (RT):

236 ~303K, 313K and 323 K). The corresponding Tafel plots are shown in (**d**). (**e**) LSV curves of

237 IrO_2 with and without a constant magnetic field (10000 Oe) under the different temperatures

238 (room temperature (RT): ~303K, 313K and 323 K). The corresponding Tafel plots are shown

239 in (**f**). Tafel slopes at various temperatures are summarized in (**g**).

240

241 The electron transfer at the catalytic interface depends on the transition probability, which is

242 associated with the wavefunction integral between OH^- and the active site. As revealed by our

243 previous work, the octahedral sites are mainly responsible to the OER[55]. The extended X-ray

244 absorption fine structure (EXAFS) showed the perfect inverse spinel structure of $CoFe_2O_4$

245 (Supplementary Figure 7). The Fe^{3+} ions distribute equally in octahedral and tetrahedral sites

246 and Co^{2+} ions distribute in octahedral sites. We further calculated the effective magnetic

247 moment (μ_{eff}) of $CoFe_2O_4$ to be about 3.44 μ_B by Curie−Weiss fitting (Supplementary Figure

248 8). The μ_{eff} for $CoFe_2O_4$ is very close to the idea value of the inverse spinel. [56] Thus, the Co^{2+}

249 ions in octahedral sites contribute to the effective ferromagnetic moment. Those results are

250 consistent in previous experimental work.[57] Considering that only Co in octahedral sites

251 contribute the effective magnetic moment, the magnetic field enhanced OER should mainly

252 happen on the Co sites. Thus, we studied the Co sites as the active sites in this work. For a

253 ferromagnetic (FM) catalyst, the orbitals of the FM oxides create an intrinsically degenerate

254 spin-polarized metallic state that optimizes the wavefunction based on the inter-atomic

255 reduction of the electron-electron repulsion. DFT calculations were performed to explore the

256 diffierent elctron structure of $CoFe_2O_4$ under an applied magnetic field (The computational

257 details are shown in the Supplementary Information). As shown in the projected density of

258 states (PDOS) of $CoFe_2O_4$ (Figure 4a), the 3d-2p hybridization of the $CoFe_2O_4$ become stronger

259 after aligning the spins. As well, compared to the $CoFe_2O_4$ with anti-parallel couplings, the

260 $CoFe_2O_4$ with spin alignment has a higher spin density on the oxygen atoms (Figure 4b). The

261 calculation indicates that the magnetic moment of the ligand hole in $CoFe_2O_4$ is 0.059 μB

262 without spin alignment and is 0.188 μB with spin alignment, which indicates a FM ligand hole

263 in $CoFe_2O_4$. A concomitant increment of the 3d-2p hybridization associate with FM ligand

264 holes will facilitate spin-selected charge transport and optimize the kinetics of the spin-charge

265 transfer in the three-phase interface.[43, 58] Thus, the dominant FM exchange between the

266 ferromagnetic catalyst and the adsorbed oxygen species (reactants) will happen (Figure 4c and

267 Supplementary Figure 9) with smaller electron-electron repulsion, which induce spin-

268 dependent conductivity and decrease the rate-limiting bonding energies, making that the first

269 electron transfer is no longer the RDS. We further prepared the Pourbaix diagram of $CoFe_2O_4$

270 as shown in Figure 4d, which show that the surface termination of $CoFe_2O_4$ is oxygen

271 termination under OER conditions. The reaction started between a ligand oxygen on the surface

272 and the adsorbed oxygen species (OH^-), and the "first" electron transfer step is $O^* + OH^- \rightarrow$

273 $*OOH + e^-$. The spin-related OER mechanisms show in Figure 4e. The FM $CoFe_2O_4$ with FM

274 ligand hole will form oxygen termination with fixed spin direction. The first electron transfer

275 process led to the generation of $O(\downarrow)^-$, that is, the first electron transfer step is spin polarization

276 process to form the triplet state intermediate $O(\downarrow)O(\downarrow)H$ species with a lower barrier

277 (Supplementary Figure 10). Consequently, the triplet state intermediate $O(\downarrow)O(\downarrow)H$ species will

278 prefer to generate the triplet state O_2. We also conducted a DFT study on the free energies of

279 OER steps on the (111) surface of $CoFe_2O_4$ with and without spin alignment. The (111) surface

280 is chosen because the TEM investigation found the surface is rich in (111) and there is no

281 remarkbale change on the surface after OER (Supplementary Figure 11). The energy diagram

282 for these two paths to produce triplet oxygen is shown in Figure 4f. The active sites with spin

283 alignment are more thermodynamically favourable to OER, if they associate with ferromagnetic

284 ligand holes,[58] and the overpotential of producing triplet oxygen is reduced by 390 mV

285 compared to that without aligning spin. The coordinated inter-atomic aligned spin on active

286 sites plays an important role in optimizing the spin-dependent reaction coordinates.
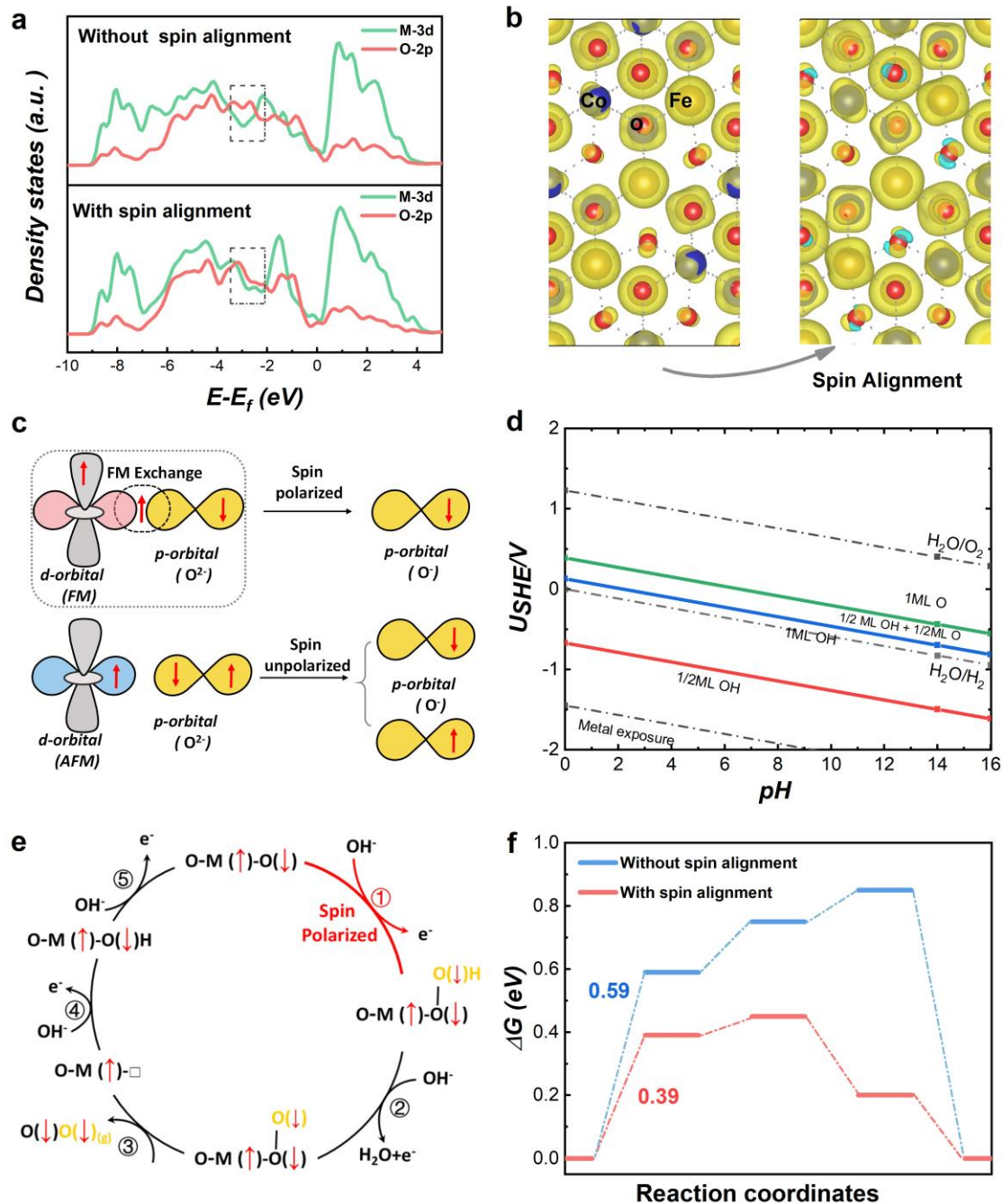
Figure 4 | Spin-polarized OER. (**a**) The projected density of states (PDOS) of CoFe2O4 without and with spin alignment. (**b**) The spin density for $CoFe_2O_4$ with and without spin alignment. (**c**) Schematic of spin-exchange mechanism for OER. The first electron transfer step is promoted by spin polarization through the FM exchange (QSEI), which gives smaller electronic repulsions and makes the adsorbed O species have a fixed spin direction. (**d**) The calculated Pourbaix diagram of the (111) surface of $CoFe_2O_4$. (**e**) The spin polarization

294   mechanisms in OER with starting from the step of O* + OH⁻ → *OOH + e⁻ step. (**f**) The free

295   energy diagram of OER at 1.23 V (vs. RHE) with and without the spin alignment on the (111)

296   surface of $CoFe_2O_4$ toward triplet oxygen production.

297

298

299   It is worth noting that OER requires the generation of paramagnetic O_2 molecules starting from

300   diamagnetic species (OH⁻ and H_2O). For a reaction involving non-magnetic molecules only, not

301   impact significantly on the reaction kinetics. We investigated the methanol oxidation reaction

302   (MOR) and ethylene glycol oxidation reaction (EGOR) on $CoFe_2O_4$ under the magnetic field.

303   Here, changes in FM catalyst conductivity caused by magnetic fields can be ignored because

304   that AB mediator is also mixed with $CoFe_2O_4$ for their application as the electrode, which

305   dominant the electron conduction. Figure 5 reveals that there is no remarkable difference in

306   these reactions under the magnetic field. This is because the reactants, intermediates, and the

307   products in these reactions are diamagnetic and there is no spin-selected electron transfer

308   between the active metal site and the adsorbed reaction species.
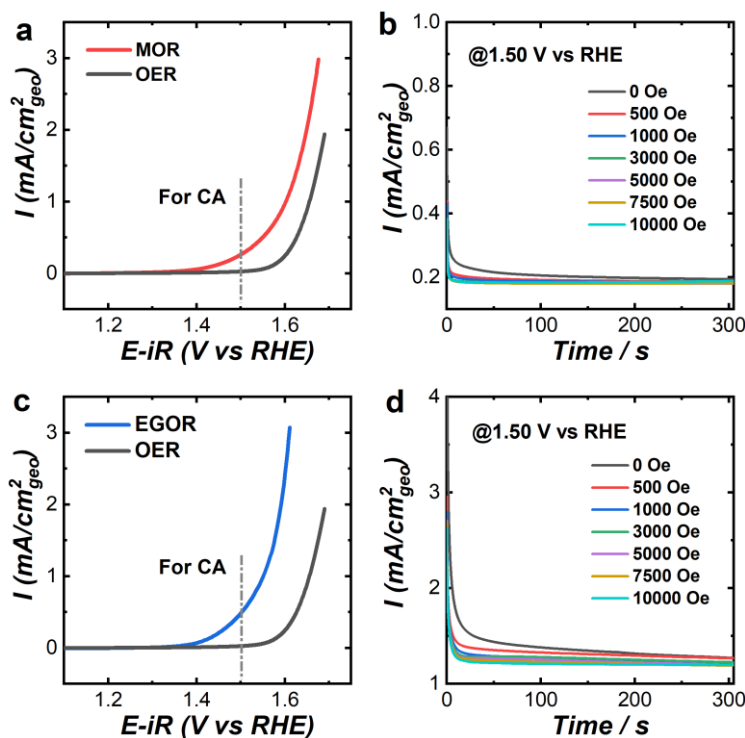
309

310   **Figure 5 | No influence on MOR and EGOR. (a)** Linear sweep voltammetry (LSV) curves of

MOR at a scan rate of 10 mV/s in 1 M KOH in the presence of 1 ml methanol. (**b**) Chronoamperometry (CA) experiments of MOR were performed at a constant potential of 1.50 V (versus RHE). (**c**) LSV curves of EGOR at a scan rate of 10 mV/s in 1 M KOH in the presence of 1 ml ethylene glycol. (**d**) The CA curves of EGOR at 1.50 V vs. RHE.

The effect of gradient magnetic field, remanence, and demagnetization

It is known that for ferromagnetic materials, the magnetic moment pertains to the spin. The more ordered its magnetic moment is, the higher the degree of positive spin polarization is. As observed in the initial magnetization curve of $CoFe_2O_4$ (Figure 6a), its magnetic moments become more orderly as the magnetic field increases, before reaching the saturation field. We then investigated the effect of the gradient magnetic field on OER activity. We carried out a series of CA measurements under the different magnetic field strength at a constant potential of 1.66, 1.66, and 1.56 V (versus RHE) for $CoFe_2O_4$, Co_3O_4, and IrO_2 respectively (Figure 6b). It can be seen that the current density of the ferromagnetic catalyst $CoFe_2O_4$ increases with the increase of the magnetic field strength. For non-ferromagnetic Co_3O_4 and IrO_2, there is almost no change when changing the field strength. The increment of the current density is summarized in Figure 6c. The increase of spatial spin polarization related to the degree of magnetization shows a positive correlation with the enhancement of the OER for ferromagnetic $CoFe_2O_4$. We also measured the LSV curves of all oxides before and after the CA experiment. As seen in Supplementary Figure 12, the OER performance ferromagnetic $CoFe_2O_4$ can be further improved after the CA test under magnetic field, but not for non-ferromagnetic Co_3O_4 and IrO_2. An interesting finding is that the OER performance of $CoFe_2O_4$ remains even after the magnetic field is removed (Figure 6d). This is because the magnetic moment is still aligned in magnetized $CoFe_2O_4$ (Figure 6e) after removing the magnetic field, which persists as the spin polarizer to create spin polarization. This is an important fact to make clear that the enhancement is due to the indirect (strong) QSEI, and not due to weak direct spin-spin interactions from the external field, a typically conceptual error. More interestingly, when the magnetized $CoFe_2O_4$ was demagnetized using an oscillating magnetic field (Figure 6g), the OER performance of $CoFe_2O_4$

339 reverted to the initial value before the field was applied. The Tafel slope of $CoFe_2O_4$ is back to

340 120 mV dec^{-1}, indicating the first electron transfer of the adsorbed OH$^-$ is again the RDS, same

341 as the status without the magnetic field. Based on the above results, we can confirm that the

342 spin polarization facilitated OER is reversible and adjustable.
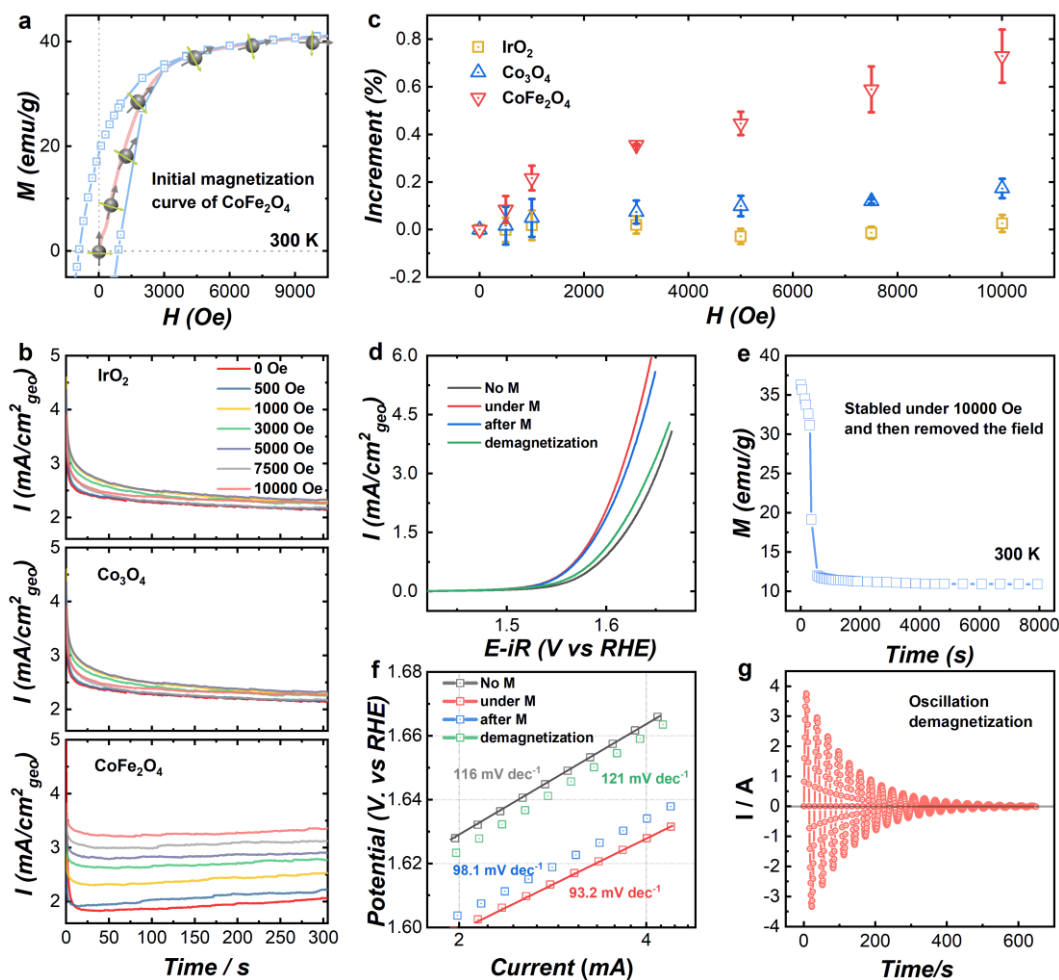
343

344 **Figure 6 | The effect of gradient magnetic field, remanence, and demagnetization. (a)**

345 Initial magnetization curve of $CoFe_2O_4$. (**b**) CA test in 1 M KOH under the different magnetic

346 field strength (0, 500, 1000, 3000, 5000, 7500, and 10000 Oe) at a constant potential of 1.66 V

347 versus RHE for $CoFe_2O_4$, Co_3O_4, and 1.56V versus RHE for IrO_2. (**c**) The increment of the

348 current density under different magnetic field strength. It was calculated by the following

349 equation: Increment (%) = ($j_M - j_{M=0}$) / $j_{M=0}$; j_M is the chronopotentiometry current density values

350 obtained under the applied magnetic fields (0, 500, 1000, 3000, 5000, 7500, and 10000 Oe).

351 The error bar represents three independent tests. (**d**) LSV curves of $CoFe_2O_4$ at a scan rate of

352 10 mV/s in O_2-saturated 1 M KOH with and without a constant magnetic field (10000 Oe), after

353 the magnetic field removed (after M), and after demagnetization. The corresponding Tafel plots

354 are shown in (**f**). (**e**) The magnetization of $CoFe_2O_4$ after removing a constant magnetic field of

355 10000 Oe. (**g**) The curve of demagnetization for $CoFe_2O_4$.

356

357

358

359 **Conclusion**

360 In summary, we have found that ferromagnetic $CoFe_2O_4$ as the spin polarizer facilitates the spin

361 polarization under a constant magnetic field, because macroscopic ferromagnetic QSEI

362 promote the OER activity. The increase of spatial spin polarization shows a positive correlation

363 with the enhancement of spin-transport (selection) during OER. We have found that the Tafel

364 slope of overall ferromagnetic $CoFe_2O_4$ switched from ~120 to ~90 mV·dec^{-1} after applying a

365 magnetic field. It indicates the change of the RDS of OER reaction under an external magnetic

366 field, i.e., the first electron transfer step is no longer the RDS. The spin-polarized electron

367 exchange between the ferromagnetic $CoFe_2O_4$ and the adsorbed oxygen species (reactants) for

368 the first electron transfer is ferromagnetic exchange under the principle of spin angular

369 momentum conservation, which leads to faster reaction kinetics for the first electron transfer

370 step. In contrast, such a phenomenon was not observed on non-ferromagnetic catalysts. The

371 findings imply that the conservation of the total spin on the active sites during OER is an

372 important concept, which applies quantum spin-exchange interactions to optimize reaction

373 kinetics. The kinetic improvements maintain after the removal of the external magnetic field,

374 and our work proves that a new path is available in the development of clean and more efficient

375 catalysts for hydrogen economy.

376

377

378 **Methods**

379 **Oxides synthesis.** Spinel $CoFe_2O_4$ oxides were synthesized by a modified conventional solid-

380 state chemistry method as described elsewhere[45] with $Fe(NO_3)_2$ and $Co(NO_3)_2$ as precursors. 9

381   mmol mixture of $Fe(NO_3)_3 \cdot 9H_2O$ (Alfa Aesar) and $Co(NO_3)_2 \cdot 6H_2O$ (Sigma Aldrich) was

382   dissolved in 15 mL of DI water, followed by stirring and vaporizing in oven at 80 °C. The

383   resulting slurry was calcinated at 250 °C for 2 hours in the air to decompose nitrous completely.

384   After grinding, the black oxide powders underwent calcination in air at 400 °C for 8 hours.

385   Co_3O_4 oxides were synthesized by the same method.

386

387   **Electrochemical characterization.** The OER tests were operated in a three-electrode cell with

388   a working electrode (WE) of glassy carbon flake (10 mm × 20 mm× 0.5 mm; Effective electrode

389   area: 1.0 cm^2), a counter electrode of platinum foil, and a Hg/HgO reference electrode (RE)

390   (filled with 1M KOH solution). The catalysts electrode was fabricated by the recipe drop-castes

391   method which was reported in elsewhere[59]. The catalysts were mixed with acetylene black (AB)

392   at a mass ration of 5:1, then were dispersed in isopropanol/water (v/v=1:4) solvent followed by

393   the addition of Na^+-exchanged Nafion as the binder. The mixtures were ultrasonicated for 30

394   min to reach homogeneous ink. The concentration of oxides in ink is 5 mg/ml, and AB is 1

395   mg/ml. Before drop-casting, the glassy carbon electrodes were polished to a mirror finish with

396   α-Al_2O_3 (50 nm) and washed by IPA and water to clean up completely. Finally, the as-prepared

397   ink (100 ul) was dropped onto glassy carbon electrodes to reach a loading mass of 500 μg_{ox} cm$^-$

398   ^{2} and the electrodes were dried overnight at room temperature. Cyclic voltammograms (CVs),

399   linear sweep voltammetry (LSV) and chronoamperometry (CA) were performed in O_2-

400   saturated 1 M KOH by using Bio-logic SP 150 potentiostat. All potentials were converted to

401   RHE scale according to the following equation: RHE = Hg/HgO + 0.098 with iR correction.

402   The tests of methanol oxidation reaction (MOR) and ethylene glycol oxidation reaction (EGOR)

403   on CFO electrodes are similar to the OER test. The difference is that the MOR and EGOR were

404   studied in 1M KOH 100 ml electrolyte in the presence of 1 ml methanol and 1ml ethylene

405   glycol, respectively[60].

406

407   **Materials characterization.** The X-ray diffraction (XRD) of oxides were carried on Bruker

408   D8 diffractometer at a scanning rate of 2° min^{-1}, under Cu-K$_\alpha$ radiation (λ = 1.5418 Å). DC

409   magnetization measurements were performed on a Superconducting Quantum Design (SQUID)

410   magnetometer (MPMS-XL). The SQUID measurements of the magnetization of samples as a

411   function of the magnetic field were carried out at 300 K in fields between -5 T and +5 T. The

412   high-resolution transmission electron microscopy (HRTEM) was carried JEOL JEM- 2100 plus

413   microscope at 200KV. The STEM results presented here were obtained using the 200kV JEOL

414   ARM electron microscope equipped (JEOL, Tokyo, Japan) with double aberration correctors,

415   a dual-energy-loss spectrometer and a cold field emission source. The atomic-resolved STEM

416   images were collected with a condense aperture of 28 mrad and a collection angle of $90 - 370$

417   mrad for HAADF and $11 - 23$ mrad for ABF images. The XPS measurements were performed

418   using PHI-5400 equipment with Al Kα beam source (250 W) and a position-sensitive detector

419   (PSD) was used to determine the surface composition of the materials. The Fourier transform

420   infrared spectroscopy–Raman spectroscopy was carried with a confocal Raman microscope

421   (Horiba HR Evolution), equipped with a diode laser emitting at 532 nm. The nominal laser

422   power was filtered down to 1mW to avoid sample overheating. Spectra were recorded with the

423   accumulation time of 60 s.

424

425   **DFT studies.** All the density functional theory (DFT) calculations were performed by Vienna

426   Ab-initio Simulation Package[61, 62] (VASP), employing the Projected Augmented Wave[63] (PAW)

427   method. The revised Perdew-Burke-Ernzerhof (RPBE) functional was used to describe the

428   exchange and correlation effects.[64-66] The GGA + U calculations are performed using the model

429   proposed by Dudarev et al.[67], with the U_{eff} (U_{eff} = Coulomb U – exchange J) values of 3.3 eV

430   and 4 eV for Co and Fe, respectively. For all the geometry optimizations, the cutoff energy was

431   set to be 500 eV. A 3×3×1 Monkhorst-Pack grids[68] was used to carry out the surface calculations

432   on the (111) surface of $CoFe_2O_4$. At least 20 Å vacuum layer was applied in z-direction of the

433   slab models, preventing the vertical interactions between slabs.

434   In alkaline conditions, OER could occur in the following four elementary steps:

435      $OH^- + * \rightarrow *OH + e^-$

436      $*OH + OH^- \rightarrow *O + H_2O + e^-$

437      $*O + OH^- \rightarrow *OOH + e^-$

438      $*OOH + OH^- \rightarrow * + O_2 + H_2O + e^-$
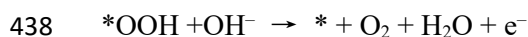
439 where * denotes the active sites on the catalyst surface. Based on the above mechanism, the

440 free energy of three intermediate states, *OH, *O, and *OOH, are important to identify a given

441 material's OER activity. The computational hydrogen electrode (CHE) model[69] was used to

442 calculate the free energies of OER, based on which the free energy of an adsorbed species is

443 defined as

444 $\Delta G_{ads} = \Delta E_{ads} + \Delta E_{ZPE} - T\Delta S_{ads}$

445 where ΔE_{ads} is the electronic adsorption energy, ΔE_{ZPE} is the zero point energy difference

446 between adsorbed and gaseous species, and $T\Delta S_{ads}$ is the corresponding entropy difference

447 between these two states. The electronic binding energy is referenced as ½ H_2 for each H atom,

448 and ($H_2O - H_2$) for each O atom, plus the energy of the clean slab. The corrections of zero point

449 energy and entropy of the OER intermediates can be found in the Supplementary Table 2.

450

451 **References**

452 1.   Young, J.L. et al. Direct solar-to-hydrogen conversion via inverted metamorphic multi-junction
453   semiconductor architectures. *Nature Energy* **2**, 17028 (2017).
454 2.   Aurbach, D., McCloskey, B.D., Nazar, L.F. & Bruce, P.G. Advances in understanding mechanisms
455   underpinning lithium–air batteries. *Nature Energy* **1**, 16128 (2016).
456 3.   Duan, C. et al. Highly durable, coking and sulfur tolerant, fuel-flexible protonic ceramic fuel
457   cells. *Nature* **557**, 217-222 (2018).
458 4.   Cheng, W. et al. Lattice-strained metal–organic-framework arrays for bifunctional oxygen
459   electrocatalysis. *Nature Energy* **4**, 115-122 (2019).
460 5.   Koshikawa, H. et al. Single Nanometer-Sized NiFe-Layered Double Hydroxides as Anode Catalyst
461   in Anion Exchange Membrane Water Electrolysis Cell with Energy Conversion Efficiency of 74.7%
462   at 1.0 A/ cm^2. *ACS Catalysis* **10**, 1886-1893 (2020).
463 6.   Stoerzinger, K.A., Qiao, L., Biegalski, M.D. & Shao-Horn, Y. Orientation-Dependent Oxygen
464   Evolution Activities of Rutile IrO_2 and RuO_2. *J.Phys. Chem. Lett.* **5**, 1636-1641 (2014).
465 7.   Hong, W.T. et al. Toward the rational design of non-precious transition metal oxides for oxygen
466   electrocatalysis. *Energy & Environmental Science* **8**, 1404-1427 (2015).
467 8.   Calle-Vallejo, F. et al. Number of outer electrons as descriptor for adsorption processes on
468   transition metals and their oxides. *Chemical Science* **4**, 1245-1249 (2013).
469 9.   Man, I.C. et al. Universality in Oxygen Evolution Electrocatalysis on Oxide Surfaces.
470   *ChemCatChem* **3**, 1159-1165 (2011).
471 10.   Suntivich, J., May, K.J., Gasteiger, H.A., Goodenough, J.B. & Shao-Horn, Y. A perovskite oxide
472   optimized for oxygen evolution catalysis from molecular orbital principles. *Science* **334**, 1383-

473   1385 (2011).

474 11. Chao, W. et al. Cations in Octahedral Sites: A Descriptor for Oxygen Electrocatalysis on
475   Transition-Metal Spinels. *Adv. Mater.* **29**, 1606800 (2017).

476 12. Suntivich, J. et al. Design principles for oxygen-reduction activity on perovskite oxide catalysts
477   for fuel cells and metal-air batteries. *Nat Chem* **3**, 546-550 (2011).

478 13. Tingbin Lim, J.W.H.N., and Jose Gracia Layered Antiferromagnetic Ordering in the Most Active
479   Perovskite Catalysts for the Oxygen Evolution Reaction. *ChemCatChem* **8**, 2968 –2974 (2016).

480 14. Ryan Sharpe, J.M., Tingbin Lim, Yunzhe Jiao, J. W. Niemantsverdriet, Victor Polo, and Jose
481   Gracia Orbital Physics of Perovskites for the Oxygen Evolution Reaction. *Top. Catal.* **61**, 267–
482   275 (2018).

483 15. Sharpe, R., Lim, T., Jiao, Y., Niemantsverdriet, J.W.H & Gracia, J. Oxygen Evolution Reaction on
484   Perovskite Electrocatalysts with Localized Spins and Orbital Rotation Symmetry. *ChemCatChem*
485   **8**, 3762-3768 (2016).

486 16. Gracia, J. et al. Analysis of the Magnetic Entropy in Oxygen Reduction Reactions Catalysed by
487   Manganite Perovskites. *ChemCatChem* **9**, 3358-3363 (2017).

488 17. Chretien, S. & Metiu, H. O_2 evolution on a clean partially reduced rutile TiO_2(110) surface and
489   on the same surface precovered with Au1 and Au2: the importance of spin conservation. *J.*
490   *Chem. Phys.* **129**, 074705 (2008).

491 18. Torun, E., Fang, C.M., de Wijs, G.A. & de Groot, R.A. Role of Magnetism in Catalysis: RuO_2 (110)
492   Surface. *J. Phys. Chem. C* **117**, 6353-6357 (2013).

493 19. Nazmutdinov, R.R., Santos, E. & Schmickler, W. Spin effects in oxygen electrocatalysis: A
494   discussion. *Electrochem. Commun.* **33**, 14-17 (2013).

495 20. A. V. Ramos, T.S.S., G. X. Miao, M.-J. Guittet, J.-B. Moussy, and J. S. Moodera Influence of
496   oxidation on the spin-filtering properties of $CoFe_2O_4$ and the resultant spin polarization. *Phys.*
497   *Rev. B* **78**, 180402 (2008).

498 21. Zhi-Min Liao, Y.-D.L., Jun Xu, Jing-Min Zhang, Ke Xia, and Da-Peng Yu Spin-Filter Effect in
499   Magnetite Nanowire. *Nano Lett.* **6**, 1087-1091 (2006).

500 22. Gracia, J. Itinerant Spins and Bond Lengths in Oxide Electrocatalysts for Oxygen Evolution and
501   Reduction Reactions. *J. Phys. Chem. C* **123**, 9967-9972 (2019).

502 23. Gracia, J., Sharpe, R. & Munarriz, J. Principles determining the activity of magnetic oxides for
503   electron transfer reactions. *J. Catal.* **361**, 331-338 (2018).

504 24. Gracia, J. Spin dependent interactions catalyse the oxygen electrochemistry. *Phys. Chem. Chem.*
505   *Phys.* **19**, 20451-20456 (2017).

506 25. Mtangi, W. et al. Control of Electrons' Spin Eliminates Hydrogen Peroxide Formation During
507   Water Splitting. *J. Am. Chem. Soc.* **139**, 2794-2798 (2017).

508 26. Zhang, W., Banerjee-Ghosh, K., Tassinari, F. & Naaman, R. Enhanced Electrochemical Water
509   Splitting with Chiral Molecule-Coated Fe_3O_4 Nanoparticles. *ACS Energy Letters* **3**, 2308-2313
510   (2018).

511 27. Mondal, P.C., Fontanesi, C., Waldeck, D.H. & Naaman, R. Spin-Dependent Transport through
512   Chiral Molecules Studied by Spin-Dependent Electrochemistry. *Acc. Chem. Res.* **49**, 2560-2568
513   (2016).

514 28. Jiao, Y., Sharpe, R., Lim, T., Niemantsverdriet, J.W.H & Gracia, J. Photosystem II Acts as a Spin-
515   Controlled Electron Gate during Oxygen Formation and Evolution. *J. Am. Chem. Soc.* **139**,

516   16604-16608 (2017).

517   29.   Lüders, U. et al. Spin filtering through ferrimagnetic $NiFe_2O_4$ tunnel barriers. *Appl. Phys. Lett.*
518   **88**, 082505 (2006).

519   30.   Garcés-Pineda, F.A., Blasco-Ahicart, M., Nieto-Castro, D., López, N. & Galán-Mascarós, J.R.
520   Direct magnetic enhancement of electrocatalytic water oxidation in alkaline media. *Nature*
521   *Energy* **4**, 519-525 (2019).

522   31.   Yiyun Yang, K.M.G., Henry S. White, and Shaowei Chen Magnetoelectrochemistry of
523   Nitrothiophenolate-Functionalized Gold Nanoparticles. *Langmuir* **19**, 9446-9449 (2003).

524   32.   Monzon, L.M.A. & Coey, J.M.D. Magnetic fields in electrochemistry: The Kelvin force. A mini-
525   review. *Electrochem. Commun.* **42**, 42-45 (2014).

526   33.   Monzon, L.M.A. & Coey, J.M.D. Magnetic fields in electrochemistry: The Lorentz force. A mini-
527   review. *Electrochem. Commun.* **42**, 38-41 (2014).

528   34.   Olivier Devos, O.A., Jean-Paul Chopart, and Alain Olivier Is There a Magnetic Field Effect on
529   Electrochemical Kinetics? *J. Phys. Chem. A* **104**, 1544-1548 (2000).

530   35.   Gatard, V., Deseure, J. & Chatenet, M. Use of magnetic fields in electrochemistry: a selected
531   review. *Current Opinion in Electrochemistry* **23**, 96-105 (2020).

532   36.   Monzon, L.M.A., Nair, V., Reilly, B. & Coey, J.M.D. Magnetically-Induced Flow during
533   Electropolishing. *J. Electrochem. Soc.* **165**, E679-E684 (2018).

534   37.   Lee du, H., Choi, C.H., Choi, T.H., Sung, B.J. & Kang, H. Asymmetric Transport Mechanisms of
535   Hydronium and Hydroxide Ions in Amorphous Solid Water: Hydroxide Goes Brownian while
536   Hydronium Hops. *J.Phys. Chem. Lett.* **5**, 2568-2572 (2014).

537   38.   Chappert, C., Fert, A. & Van Dau, F.N. The emergence of spin electronics in data storage. *Nat.*
538   *Mater.* **6**, 813-823 (2007).

539   39.   Binasch, G., Grunberg, P., Saurenbach, F. & Zinn, W. Enhanced magnetoresistance in layered
540   magnetic structures with antiferromagnetic interlayer exchange. *Phys Rev B Condens Matter*
541   **39**, 4828-4830 (1989).

542   40.   Zhou, B.H. & Rinehart, J.D. A Size Threshold for Enhanced Magnetoresistance in Colloidally
543   Prepared $CoFe_2O_4$ Nanoparticle Solids. *ACS Cent Sci* **4**, 1222-1227 (2018).

544   41.   Jun Chen, X., Soong Ju Oh, JamesM. Kikkawa, Cherie R. Kagan, and Christopher B. Murray
545   Bistable Magnetoresistance Switching in Exchange-Coupled $CoFe_2O_4$-Fe_3O_4 Binary Nanocrystal
546   Superlattices by Self-Assembly and Thermal Annealing. *ACS Nano.* **7**, 1478-1486 (2013).

547   42.   Gul, I.H. & Maqsood, A. Structural, magnetic and electrical properties of cobalt ferrites
548   prepared by the sol–gel route. *J. Alloys Compd.* **465**, 227-231 (2008).

549   43.   Xu, Z.J. From Two-Phase to Three-Phase: The New Electrochemical Interface by Oxide
550   Electrocatalysts. *Nanomicro Lett* **10**, 8 (2018).

551   44.   Xu, Z.J. Transition metal oxides for water oxidation: All about oxyhydroxides? *Science China*
552   *Materials* **63**, 3-7 (2019).

553   45.   Wu, T. et al. Iron-facilitated dynamic active-site generation on spinel $CoAl_2O_4$ with self-
554   termination of surface reconstruction for water oxidation. *Nature Catalysis* **2**, 763-772 (2019).

555   46.   Chen, Y. et al. Exceptionally active iridium evolved from a pseudo-cubic perovskite for oxygen
556   evolution in acid. *Nat. Commun.* **10**, 572-582 (2019).

557   47.   El Arrassi, A. et al. Intrinsic Activity of Oxygen Evolution Catalysts Probed at Single $CoFe_2O_4$
558   Nanoparticles. *J. Am. Chem. Soc.* **141**, 9197-9201 (2019).

559   48.   Chandramohan, P., Srinivasan, M.P., Velmurugan, S. & Narasimhan, S.V. Cation distribution and
560   particle size effect on Raman spectrum of $CoFe_2O_4$. *J. Solid State Chem.* **184**, 89-96 (2011).

561   49.   Zhou, Z. et al. Electronic structure studies of the spinel $CoFe_2O_4$ by X-ray photoelectron
562   spectroscopy. *Appl. Surf. Sci.* **254**, 6972-6975 (2008).

563   50.   Fang, Y.-H. & Liu, Z.-P. Tafel Kinetics of Electrocatalytic Reactions: From Experiment to First-
564   Principles. *ACS Catalysis* **4**, 4364-4376 (2014).

565   51.   Sun, S. et al. Switch of the Rate-Determining Step of Water Oxidation by Spin-Selected Electron
566   Transfer in Spinel Oxides. *Chem. Mater.* **31**, 8106-8111 (2019).

567   52.   Duan, Y. et al. Revealing the Impact of Electrolyte Composition for Co-Based Water Oxidation
568   Catalysts by the Study of Reaction Kinetics Parameters. *ACS Catalysis* **10**, 4160-4170 (2020).

569   53.   Craig, M.J. et al. Universal scaling relations for the rational design of molecular water oxidation
570   catalysts with near-zero overpotential. *Nature Communications* **10** (2019).

571   54.   García-Melchor, M., Vilella, L., López, N. & Vojvodic, A. Computationally Probing the
572   Performance of Hybrid, Heterogeneous, and Homogeneous Iridium-Based Catalysts for Water
573   Oxidation. *ChemCatChem* **8**, 1792-1798 (2016).

574   55.   Wei, C. et al. Cations in Octahedral Sites: A Descriptor for Oxygen Electrocatalysis on Transition-
575   Metal Spinels. *Adv. Mater.* **29**, 1606800 (2017).

576   56.   J. Teillet, F.B.a.R.K. Magnetic structure of CoFe2O4. *J. Magn. Magn. Mater.* **123**, 93-96 (1993).

577   57.   M. Guiilot, j.O., and A. Marchand High magnetic field magnetization study in cadmium-cobalt
578   ferrite single crystals. *Condens. Matter Phys.* **71**, 193-197 (1988).

579   58.   Zhang, L., Cheruvathur, A., Biz, C., Fianchini, M. & Gracia, J. Ferromagnetic ligand holes in cobalt
580   perovskite electrocatalysts as an essential factor for high activity towards oxygen evolution.
581   *Phys. Chem. Chem. Phys.* **21**, 2977-2983 (2019).

582   59.   Suntivich, J., Gasteiger, H.A., Yabuuchi, N. & Shao-Horn, Y. Electrocatalytic Measurement
583   Methodology of Oxide Catalysts Using a Thin-Film Rotating Disk Electrode. *J. Electrochem. Soc.*
584   **157**, B1263-B1268 (2010).

585   60.   Sun, S., Zhou, Y., Hu, B., Zhang, Q. & Xu, Z.J. Ethylene Glycol and Ethanol Oxidation on Spinel
586   Ni-Co Oxides in Alkaline. *J. Electrochem. Soc.* **163**, H99-H104 (2015).

587   61.   Kresse, G. & Furthmüller, J. Efficient iterative schemes for ab initio total-energy calculations
588   using a plane-wave basis set. *Phys. Rev. B* **54**, 11169-11186 (1996).

589   62.   Kresse, G. & Hafner, J. Ab initio molecular dynamics for liquid metals. *Phys. Rev. B* **49**, 14251-
590   14269 (1994).

591   63.   Blöchl, P.E. Projector augmented-wave method. *Phys. Rev. B* **50**, 17953-17979 (1994).

592   64.   Perdew, J.P., Burke, K. & Ernzerhof, M. Generalized Gradient Approximation Made Simple. *Phys.*
593   *Rev. Lett.* **77**, 3865-3868 (1996).

594   65.   Zhang, Y. & Yang, W. Comment on "Generalized Gradient Approximation Made Simple". *Phys.*
595   *Rev. Lett.* **80**, 890-890 (1998).

596   66.   Hammer, B., Hansen, L.B. & Nørskov, J.K. Improved adsorption energetics within density-
597   functional theory using revised Perdew-Burke-Ernzerhof functionals. *Phys. Rev. B* **59**, 7413-
598   7421 (1999).

599   67.   Dudarev, S., Botton, G., Savrasov, S., Humphreys, C. & Sutton, A. Electron-energy-loss spectra
600   and the structural stability of nickel oxide: An LSDA+ U study. *Phys. Rev. B* **57**, 1505 (1998).

601   68.   Monkhorst, H.J. & Pack, J.D. Special points for Brillouin-zone integrations. *Phys. Rev. B* **13**, 5188

602   (1976).

603   69.   Nørskov, J.K. et al. Origin of the overpotential for oxygen reduction at a fuel-cell cathode. *The*
604   *Journal of Physical Chemistry B* **108**, 17886-17892 (2004).

605

620

621   **Author contributions**

622   X.R., T.W. and Y.S. contribute equally to this work. Z.X., X.R., T.W. conceived the original

623   concept and designed the experiments. T.W. prepared the materials. X. R. performed most

624   characterizations and analysis. G.X. and X.R. performed the Raman spectroscopy measurement.

625   H.Y., X. R. and L.Y. carried out magnetic property measurements and analysis. Y.S. contributed

626   the DFT calculations and analysis. T.W., X.R., and Z.X. contributed the mechanism analysis.

627   J.G. contributed the explanation of QSEI theory. X.R., T.W., Y.S., H.Y., and Z.X wrote the

628   manuscript with the input from all authors. All authors engaged in the analysis of experimental

629   results and manuscript edition.

630

631   **Data availability statement**

632 The data that support the findings of this study are available from the corresponding author
633 upon reasonable request.
634
635

636 **Competing interests**

637 The authors declare no competing financial interests.

638

639 **Additional information**

640 Supplementary information is available for this paper at

641
642

Supplementary materials

Spin-polarized Oxygen Evolution Reaction under Magnetic Field

Xiao Ren[1,2], Tianze Wu[1,2,3], Yuanmiao Sun[2], Yan Li[1], Guoyu Xian[1], Xianhu Liu[4], Chengmin Shen[1], Jose Gracia[5], Hong-Jun Gao[1], Haitao Yang[1]*, Zhichuan J. Xu[2,3,6]*

[1] Beijing National Laboratory for Condensed Matter Physics and Institute of Physics, Chinese Academy of Science, P.O.Box 603, Beijing, 100190, China;

[2] School of Material Science and Engineering, Nanyang Technological University, 50 Nanyang Avenue, Singapore 639798, Singapore;

[3] Solar Fuels Laboratory, Nanyang Technological University, 50 Nanyang Avenue, Singapore 639798, Singapore;

[4] Key Laboratory of Advanced Material Processing & Mold (Zhengzhou University), Ministry of Education, Zhengzhou 450002, China;

[5] MagnetoCat SL, General Polavieja 9 3I, 03012 Alicante, Spain;

[6] Energy Research Institute @ Nanyang Technological University, 50 Nanyang Avenue, Singapore 639798, Singapore.

E-mails: xuzc@ntu.edu.sg; htyang@iphy.ac.cn

22 **Detailed Experimental Methods**

23 **Oxides synthesis.** Spinel $CoFe_2O_4$ oxides were synthesized by a modified conventional solid-state

24 chemistry method as described elsewhere[1] with $Fe(NO_3)_2$ and $Co(NO_3)_2$ as precursors. 9 mmol mixture

25 of $Fe(NO_3)_3 \cdot 9H_2O$ (Alfa Aesar) and $Co(NO_3)_2 \cdot 6H_2O$ (Sigma Aldrich) was dissolved in 15 mL of DI water,

26 followed by stirring and vaporizing in oven at 80 °C. The resulting slurry was calcinated at 250 °C for 2

27 hours in the air to decompose nitrous completely. After grinding, the black oxide powders underwent

28 calcination in air at 400 °C for 8 hours. Co_3O_4 oxides were synthesized by the same method.

29

30 **Electrochemical characterization.** The OER tests were operated in a three-electrode cell with a working

31 electrode (WE) of glassy carbon flake (10 mm × 20 mm× 0.5 mm; Effective electrode area: 1.0 cm^2), a

32 counter electrode of platinum foil, and a Hg/HgO reference electrode (RE) (filled with 1M KOH solution).

33 The catalysts electrode was fabricated by the recipe drop-castes method which was reported in elsewhere[2].

34 The catalysts were mixed with acetylene black (AB) at a mass ration of 5:1, then were dispersed in

35 isopropanol/water (v/v=1:4) solvent followed by the addition of Na^+-exchanged Nafion as the binder.

36 The mixtures were ultrasonicated for 30 min to reach homogeneous ink. The concentration of oxides in

37 ink is 5 mg/ml, and AB is 1 mg/ml. Before drop-casting, the glassy carbon electrodes were polished to a

38 mirror finish with α-Al_2O_3 (50 nm) and washed by IPA and water to clean up completely. Finally, the as-

39 prepared ink (100 ul) was dropped onto glassy carbon electrodes to reach a loading mass of 500 μg_{ox} cm$^-$

40 ^{2} and the electrodes were dried overnight at room temperature. Cyclic voltammograms (CVs), linear

41 sweep voltammetry (LSV) and chronoamperometry (CA) were performed in O_2-saturated 1 M KOH by

42 using Bio-logic SP 150 potentiostat. CA test under the different magnetic field strength (0, 500, 1000,

43 3000, 5000, 7500, and 10000 Oe) at a constant potential of 1.66 V versus RHE for $CoFe_2O_4$, Co_3O_4, and

44 1.56V versus RHE for IrO_2. All potentials were converted to RHE scale according to the following

45 equation: RHE = Hg/HgO + 0.098 with iR correction. The tests of methanol oxidation reaction (MOR)

46 and ethylene glycol oxidation reaction (EGOR) on CFO electrodes are similar to the OER test. The

47 difference is that the MOR and EGOR were studied in 1M KOH 100 ml electrolyte in the presence of 1

48 ml methanol and 1ml ethylene glycol, respectively[3].

49

50 **Materials characterization.** The X-ray diffraction (XRD) of oxides were carried on Bruker D8

51 diffractometer at a scanning rate of 2° min^{-1}, under Cu-K_α radiation (λ = 1.5418 Å). DC magnetization

52 measurements were performed on a Superconducting Quantum Design (SQUID) magnetometer (MPMS-

53 XL). The SQUID measurements of the magnetization of samples as a function of the magnetic field were

54 carried out at 300 K in fields between -5 T and +5 T. The high-resolution transmission electron

55 microscopy (HRTEM) was carried JEOL JEM- 2100 plus microscope at 200KV. The STEM results

56 presented here were obtained using the 200kV JEOL ARM electron microscope equipped (JEOL, Tokyo,

57 Japan) with double aberration correctors, a dual-energy-loss spectrometer and a cold field emission

58 source. The atomic-resolved STEM images were collected with a condense aperture of 28 mrad and a

59 collection angle of $90 - 370$ mrad for HAADF and $11 - 23$ mrad for ABF images. The XPS measurements

60 were performed using PHI-5400 equipment with Al Kα beam source (250 W) and a position-sensitive

61 detector (PSD) was used to determine the surface composition of the materials. The Fourier transform

62 infrared spectroscopy–Raman spectroscopy was carried with a confocal Raman microscope (Horiba HR

63 Evolution), equipped with a diode laser emitting at 532 nm. The nominal laser power was filtered down

64 to 1mW to avoid sample overheating. Spectra were recorded with the accumulation time of 60 s. We

65 have carried out HRTEM observation on the $CoFe_2O_4$ catalyst at the identical location before and after

66 the electrochemical reaction using identical location TEM technique (IL-TEM). The detailed methods of

67 IL-TEM are as follows. A diluted ink containing catalyst was pipetted onto the gold finder grid (400

68 mesh, TED PELLA, USA). The pristine catalyst on the gold finder grid was observed at the specific

69 location before cycling. Then the grid was used at the working electrode in an electrochemical cell. After

70 the electrochemical cycling, the grid was dried under Ar flow and observed under TEM again. The grid

71 allowed us to find the particle at the same location as it was before electrochemical cycling. The images

72 are shown in Supplementary Figure 11. It is clear that those particles remain unchanged after

73 electrochemical cycling and there is no remarkable surface change.

74

75 **DFT studies.** All the density functional theory (DFT) calculations were performed by Vienna Ab-initio

76 Simulation Package[4, 5] (VASP), employing the Projected Augmented Wave[6] (PAW) method. The revised

77 Perdew-Burke-Ernzerhof (RPBE) functional was used to describe the exchange and correlation effects.[7-

78 9] The GGA + U calculations are performed using the model proposed by Dudarev et al.[10], with the U_{eff}

79 (U_{eff} = Coulomb U – exchange J) values of 3.3 eV and 4 eV for Co and Fe, respectively. For all the

80 geometry optimizations, the cutoff energy was set to be 500 eV. A $3\times3\times1$ Monkhorst-Pack grids[11] was

81 used to carry out the surface calculations on the (111) surface of $CoFe_2O_4$. At least 20 Å vacuum layer

82 was applied in z-direction of the slab models, preventing the vertical interactions between slabs.

83 In alkaline conditions, OER could occur in the following four elementary steps:

84 $OH^- + * \rightarrow *OH + e^-$

85 $*OH + OH^- \rightarrow *O + H_2O + e^-$

86 $*O + OH^- \rightarrow *OOH + e^-$

87 $*OOH + OH^- \rightarrow * + O_2 + H_2O + e^-$
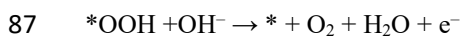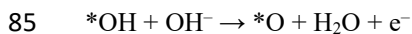
88 where * denotes the active sites on the catalyst surface. Based on the above mechanism, the free energy

89 of three intermediate states, *OH, *O, and *OOH, are important to identify a given material's OER

90 activity. The computational hydrogen electrode (CHE) model[12] was used to address the electrochemical

91 proton-electron transfer with applied potential. The free energies of each elementary step were defined

92 as

93 $\Delta G_{ads} = \Delta E_{ads} + \Delta E_{ZPE} - T\Delta S_{ads}$

94 where ΔE_{ads} is the electronic adsorption energy, ΔE_{ZPE} is the zero point energy difference between

95 adsorbed and gaseous species, and $T\Delta S_{ads}$ is the corresponding entropy difference between these two

96 states. The electronic binding energy is referenced as ½ H_2 for each H atom, and ($H_2O - H_2$) for each O

97 atom, plus the energy of the clean slab. The corrections of zero point energy and entropy of the OER

98 intermediates can be found in the Supplementary Table 2. The details of computational under magnetic

99 field are as follows. The function of the outer magnetic field is to align all the randomly oriented spin in

100 the catalyst to a specific direction. To model this situation, we have used the 'LNONCOLLINEAR' and

101 'SAXIS' keywords to make the spin in the catalyst to a specific direction. And during the calculations,

102 we did not set initial guesses of the magnetic moments and let VASP to fully relax until finding out the

103 most stable configuration. In the Supplementary Table 3, we have summarized the final magnetic

104 moments (μ_B) of the metal cations after structural optimization. The spin densities (μ_B) of the adsorbed

105 oxygen species summarized in Supplementary Table 4.

106 The surface Pourbaix diagram was calculated based on the method proposed by Hansen et al.[13], where

107 the free energy of oxygen and hydroxyl exchange at a given surface at any pH and potential is calculated

108 as

109 $$G(HO*) = \Delta G_0(HO*) - eU_{SHE} - k_B T \ln 10 \, pH + \Delta G_{field}$$

110   Where ΔG_{field} is the change in the adsorption energy due to the electric field in the electrochemical double

111   layer at the cathode. According to the work by Rossmeisl et al.[14], the relative stability change of O* and

112   OH* under electric field is sufficiently low and it is believed that the trend in adsorption energies can be

113   well described by neglecting ΔG_{field} in the construction of the surface Pourbaix diagram.

114   The term ΔG_0 is calculated by correcting the DFT energies for zero-point energies and entropy via

115    $$\Delta G_0 = \Delta E + \Delta ZPE - T\Delta S$$

116   Where ΔE and ΔZPE are the DFT energy and the change in zero-point energy of the adsorbates,

117   respectively. More details of the calculation setup can be found in reference.[13]

118

119

120

121

122

123

124

125

126

127

128

129

130

131
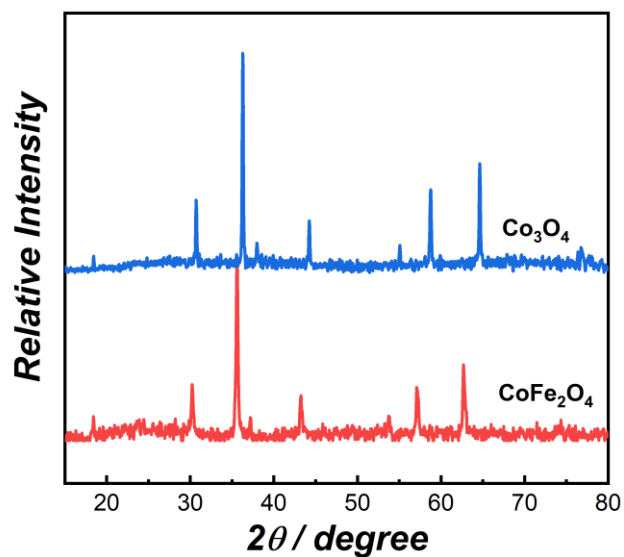
Supplementary Figure 1. The powder X-ray diffraction (XRD) patterns of as-synthesized $CoFe_2O_4$ and

Co_3O_4. The details are summarized in Table S1.

138

139
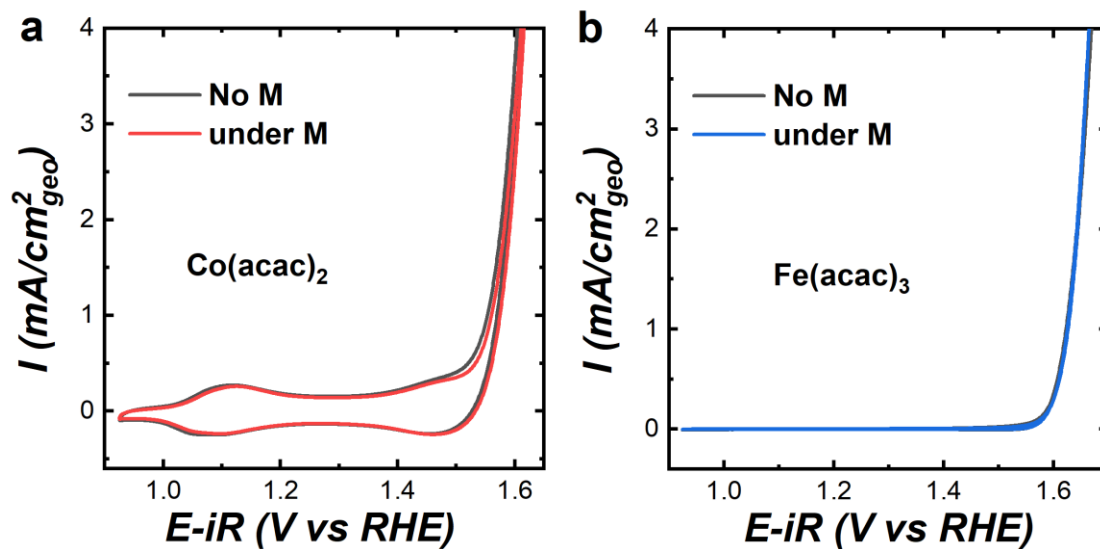
Supplementary Figure 2. Cyclic voltammetry (CV) of $Co(acac)_2$, (**a**) and $Fe(acac)_3$ (**b**) catalysts at a

scan rate of 10 mV/s in O_2-saturated 1 M KOH with and without a constant magnetic field (10000 Oe).

142

143

144

145
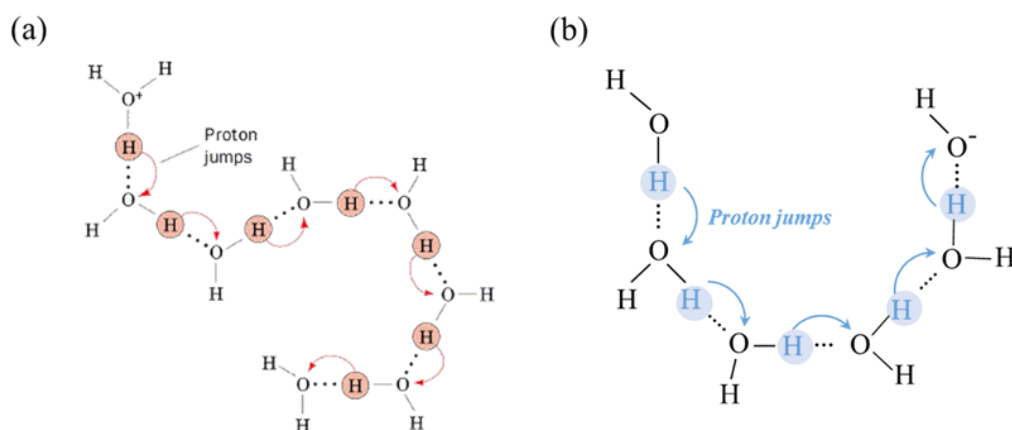
Supplementary Figure 3. The mechanism of proton hopping (jump) for (a) H_3O^+ and (b) OH^- in aqueous
solution.[15]

148

149
150
151
152
153

154
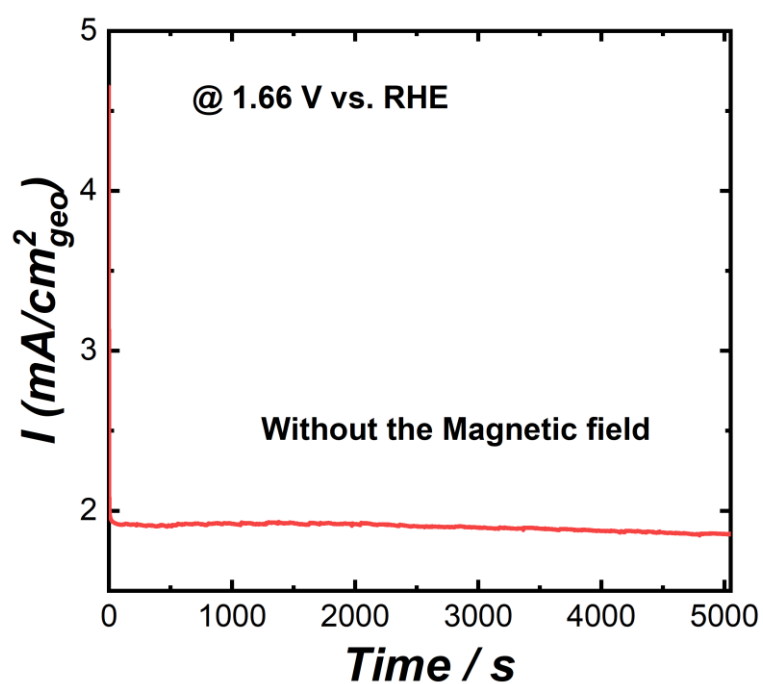
Supplementary Figure 4. CA test in 1 M KOH at a constant potential of 1.66 V versus RHE for $CoFe_2O_4$.

156

157
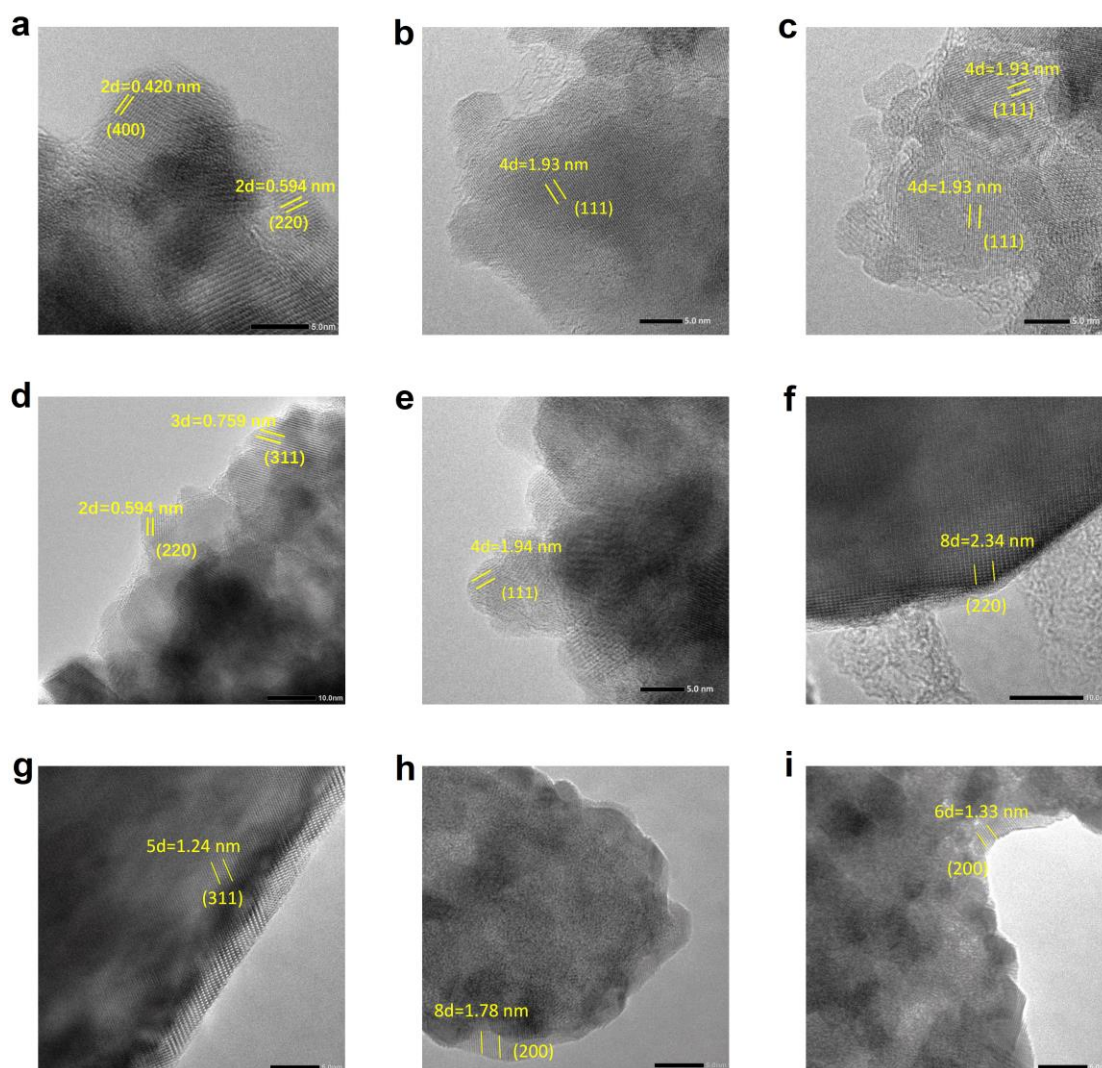
Supplementary Figure 5. HRTEM images of $CoFe_2O_4$ before (**a-c**) and after OER (**d, e**). HRTEM images of Co_3O_4 before (**f**) and after OER (**g**). HRTEM images of IrO_2 before (**h**) and after OER (**i**).

172
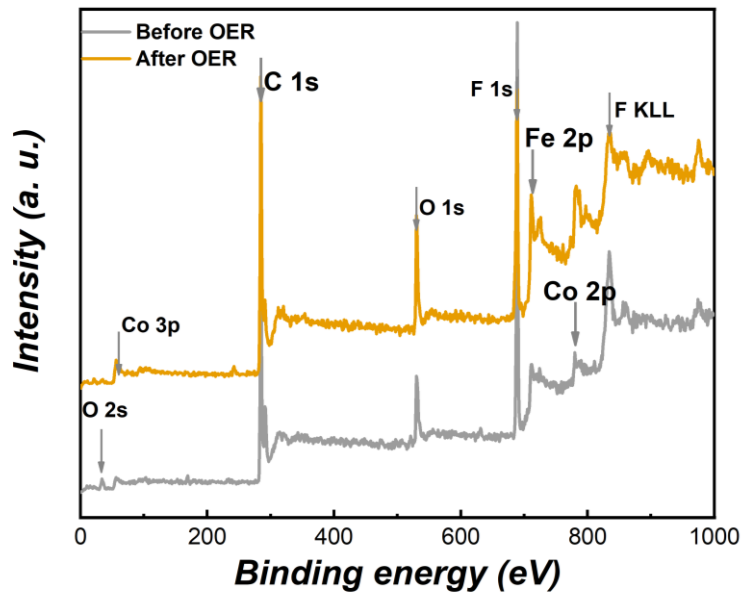
Supplementary Figure 6. The XPS survey spectra of $CoFe_2O_4$ before and after OER.

174
175
176
177
178
179
180
181
182
183
184
185
186
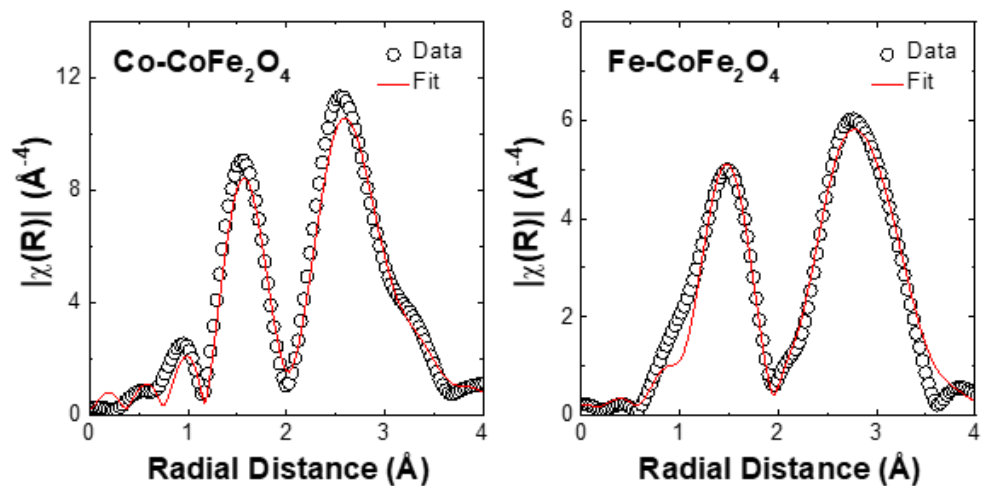
	Tetrahedral site	Octahedral site
Co_x	0.109	0.891
Co-O (Å)	1.81	2.06
Co-O coordination No.	3.3	4.9
Fe_y	0.891	1.109
Fe-O (Å)	1.93	1.99
Fe-O coordination No.	3.0	4.5
$\chi_v^2 = 376.9$; R factor = 0.0188		

187

188 **Supplementary Figure 7.** EXAFS $k^3\chi(R)$ spectra (gray circles) and fitting results (solid lines) of

189 $CoFe_2O_4$ oxides at Co and Fe K-edge. The table show the summary of EXAFS fitting results for $CoFe_2O_4$.

190 It can be seen that $CoFe_2O_4$ cubic spinels, ≈90% Co cations occupy octahedral.

191

192
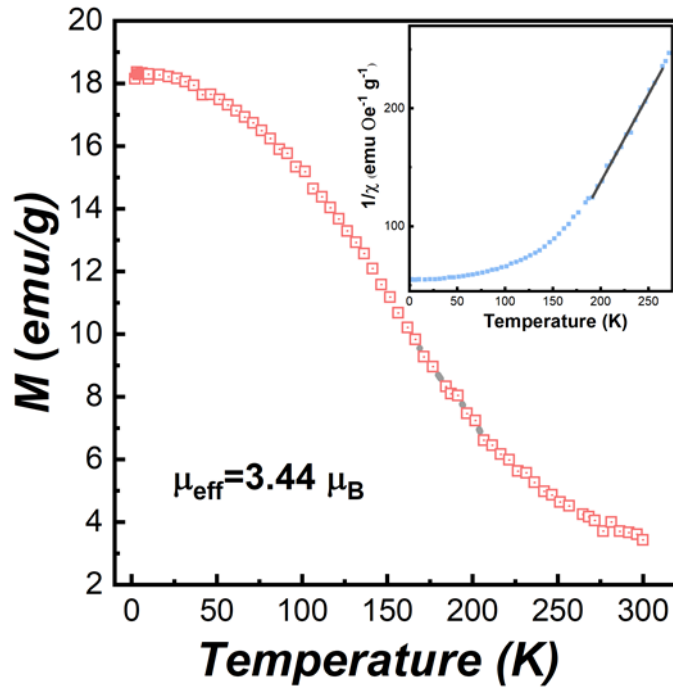
Supplementary Figure 8. The field-cooled M-T curves of $CoFe_2O_4$. The inset figure shows the temperature dependence of reciprocal susceptibilities. The solid line is the fitting results by the Curie–Weiss law. In the high temperature area, the susceptibilities derived from the magnetizations (χ = M/H) obey a Curie−Weiss law: $\chi = C/T − T_C$, where C is Curie constant, and T_C is Curie−Weiss temperature. By fitting the susceptibility versus and T data, an effective magnetic moment μ_{eff} can be obtained through $\mu_{eff} = \sqrt{8C}\ \mu_B$. Here, the calculated μ_{eff} of 3.44 μ_B for the $CoFe_2O_4$ sample is very close to the idea inverse spinel value.

220
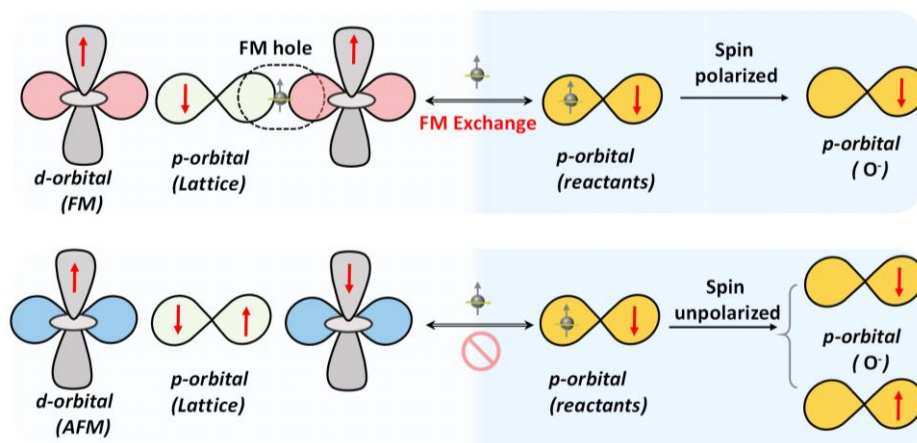
221

222 **Supplementary Figure 9.** Schematic diagram of spin electron transfer in a catalyst. FM holes present in

223 the M−O bonds and also in the oxygen ligands where the dominant FM exchange happens and enhances

224 spin-selective charge transport.

225

226

227

228

229

230
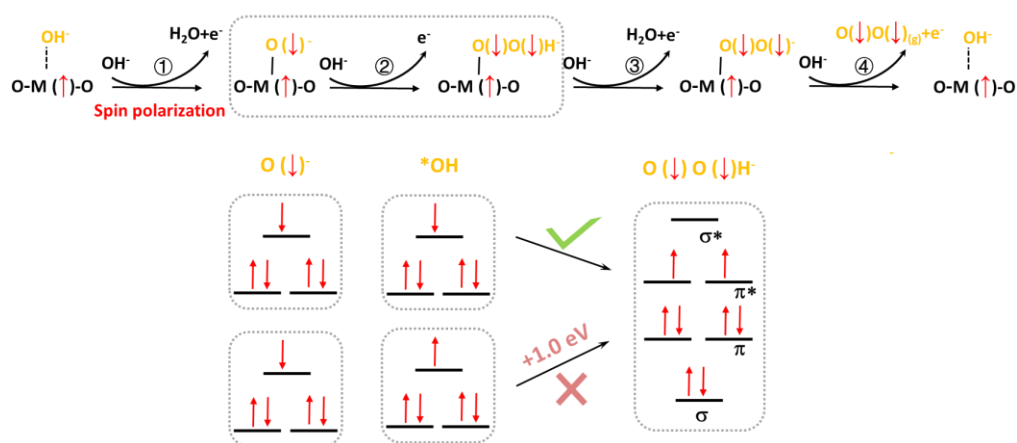
231

232 **Supplementary Figure 10.** The production of the triplet intermediate O(↓)O(↓)H species.

233

234
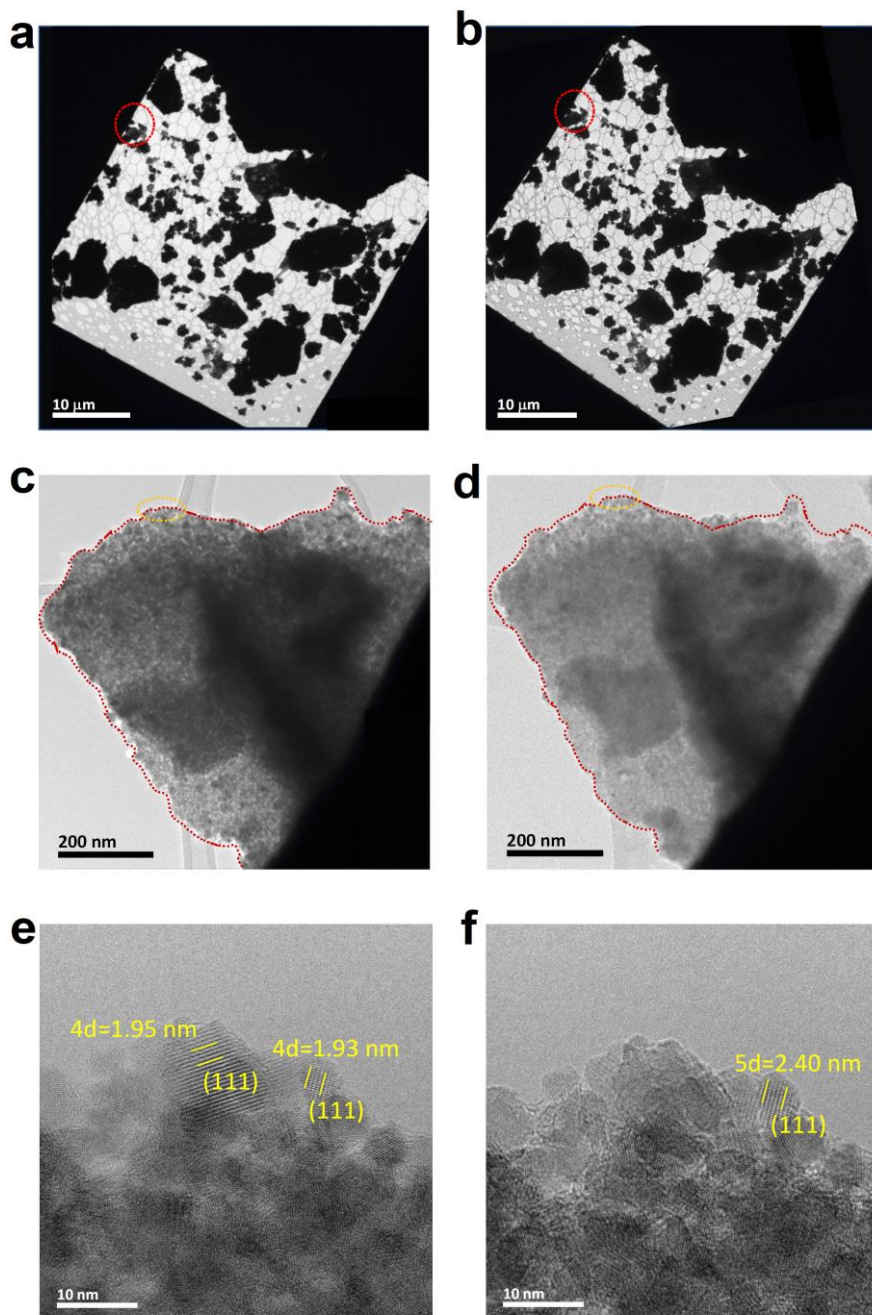
Supplementary Figure 11. Identical location TEM (IL-TEM) images of the $CoFe_2O_4$ before (**a**, **c**, and **e**) and after OER measurement (**b**, **d**, and **f**).

235

236

237

238

239

240

241

242

243

244

245

246

247
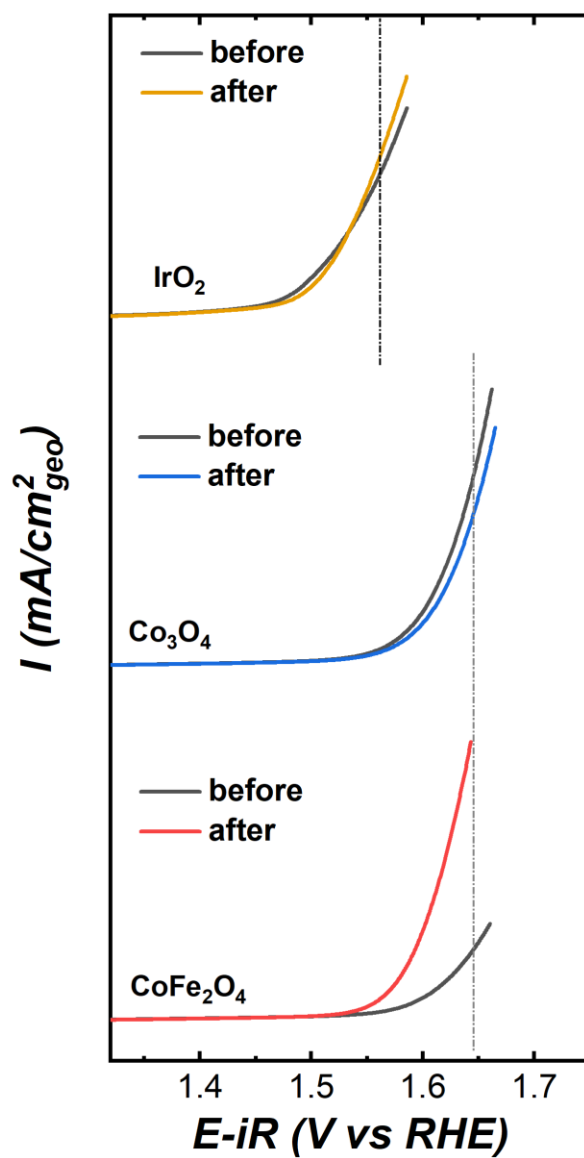
Supplementary Figure 12. Linear sweep voltammetry (LSV) of $CoFe_2O_4$, Co_3O_4, and IrO_2 catalysts at

a scan rate of 10 mV/s in O_2-saturated 1 M KOH before and after CA test.

250
251
252
253
254
255
256
257
258
259
260
261

262
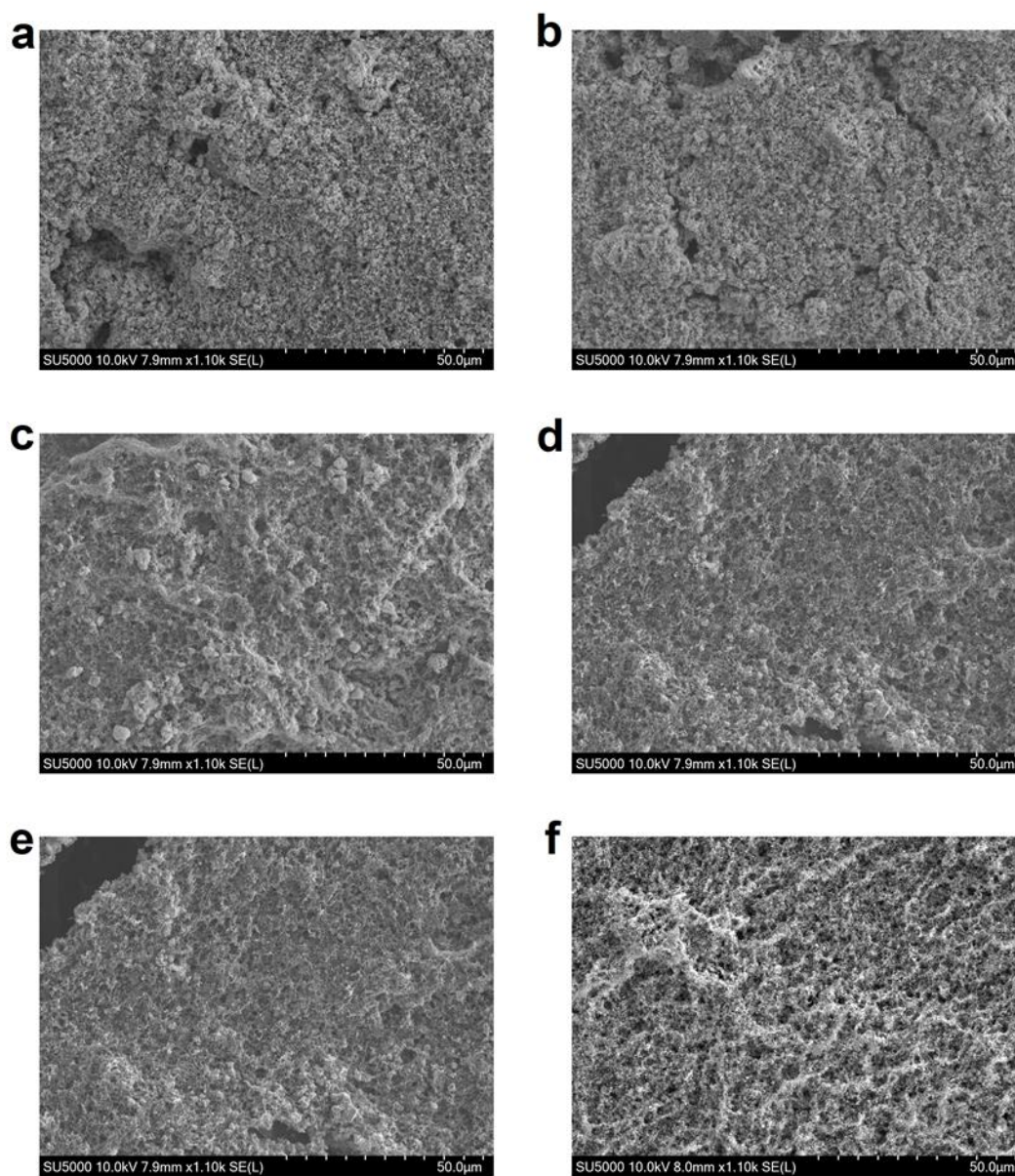
263
264 **Supplementary Figure 13.** SEM images of CoFe$_2$O$_4$ (**a**) before OER and (**b**) after OER; SEM images
265 of Co$_3$O$_4$ (**c**) before OER and (**d**) after OER; SEM images of IrO$_2$ (**e**) before OER and (**f**) after OER.
266 As shown in Supplementary Figure, the microstructure of CoFe$_2$O$_4$, Co$_3$O$_4$, and IrO$_2$ before and after
267 OER test under magnetic field have no remarkable difference observed.
268
269
270

271 **Supplementary Table 1.** Summary crystal structure parameters and magnetic data.

Samples	Crystal structure	PDF	Magnetism (300K)
$CoFe_2O_4$	Spinel (F-3dm)	22-1086	Saturation magnetization (Ms): 44 emu/gCoercivity (Hc): 887 Oe
Co_3O_4	Spinel (F-3dm)	42-1467	Magnetic susceptibility (χ): 3.07*10-5
IrO_2	Rutile (P42/mnm)	43-1019	χ: 0.51*10-6

272

273

274 **Supplementary Table 2.** The correction of zero point energy and entropy of the adsorbed and gaseous

275 species.

	ZPE (eV)	TS (eV)
*OOH	0.35	0
*O	0.05	0
*OH	0.31	0.01
H_2O	0.56	0.67
H_2	0.27	0.41

276

277

278 **Supplementary Table 3.** The magnetic moments (μ_B) of the metal cations before and after structural

279 optimization.

	Fe (Tet)	Fe (Oct)	Co (Oct)
Without aligned $CoFe_2O_4$	4.224	4.087	0.869
With aligned $CoFe_2O_4$	2.451	2.487	0.530

280

281 **Supplementary Table 4.** Calculated spin densities (μ_B) of the adsorbed oxygen species.

	*OH	*O	*OOH
Without spin alignment	0.065	0.195	O1: -0.025 O2: -0.063
With spin alignment	0.053	0.091	O1: -0.026 O2: -0.044

282

References

1. Wu, T. et al. Iron-facilitated dynamic active-site generation on spinel $CoAl_2O_4$ with self-termination of surface reconstruction for water oxidation. *Nature Catalysis* **2**, 763-772 (2019).

2. Suntivich, J., Gasteiger, H.A., Yabuuchi, N. & Shao-Horn, Y. Electrocatalytic Measurement Methodology of Oxide Catalysts Using a Thin-Film Rotating Disk Electrode. *J. Electrochem. Soc.* **157**, B1263-B1268 (2010).

3. Sun, S., Zhou, Y., Hu, B., Zhang, Q. & Xu, Z.J. Ethylene Glycol and Ethanol Oxidation on Spinel Ni-Co Oxides in Alkaline. *J. Electrochem. Soc.* **163**, H99-H104 (2015).

4. Kresse, G. & Furthmüller, J. Efficient iterative schemes for ab initio total-energy calculations using a plane-wave basis set. *Phys. Rev. B* **54**, 11169-11186 (1996).

5. Kresse, G. & Hafner, J. Ab initio molecular dynamics for liquid metals. *Phys. Rev. B* **49**, 14251-14269 (1994).

6. Blöchl, P.E. Projector augmented-wave method. *Phys. Rev. B* **50**, 17953-17979 (1994).

7. Perdew, J.P., Burke, K. & Ernzerhof, M. Generalized Gradient Approximation Made Simple. *Phys. Rev. Lett.* **77**, 3865-3868 (1996).

8. Zhang, Y. & Yang, W. Comment on "Generalized Gradient Approximation Made Simple". *Phys. Rev. Lett.* **80**, 890-890 (1998).

9. Hammer, B., Hansen, L.B. & Nørskov, J.K. Improved adsorption energetics within density-functional theory using revised Perdew-Burke-Ernzerhof functionals. *Phys. Rev. B* **59**, 7413-7421 (1999).

10. Dudarev, S., Botton, G., Savrasov, S., Humphreys, C. & Sutton, A. Electron-energy-loss spectra and the structural stability of nickel oxide: An LSDA+ U study. *Phys. Rev. B* **57**, 1505 (1998).

11. Monkhorst, H.J. & Pack, J.D. Special points for Brillouin-zone integrations. *Phys. Rev. B* **13**, 5188 (1976).

12. Nørskov, J.K. et al. Origin of the overpotential for oxygen reduction at a fuel-cell cathode. *The Journal of Physical Chemistry B* **108**, 17886-17892 (2004).

13. Heine A. Hansen, J.R.a.J.K.N. Surface Pourbaix diagrams and oxygen reduction activity of Pt, Ag and Ni(111) surfaces studied by DFT. *Phys. Chem. Chem. Phys.* **10**, 3722–3730 (2008).

14. Jan Rossmeisl, J.K.N., Christopher D. Taylor, Michael J. Janik, and Matthew Neurock Calculated Phase Diagrams for the Electrochemical Oxidation and Reduction of Water over Pt(111). *J. Phys. Chem. B* **110**, 21833-21839 (2006).

15. Lee du, H., Choi, C.H., Choi, T.H., Sung, B.J. & Kang, H. Asymmetric Transport Mechanisms of Hydronium and Hydroxide Ions in Amorphous Solid Water: Hydroxide Goes Brownian while Hydronium Hops. *J.Phys. Chem. Lett.* **5**, 2568-2572 (2014).